Analytical Predictions for Zonally Symmetric Equilibrium States of the Stratospheric Polar Vortex

RICARDO PRIETO AND WAYNE H. SCHUBERT

Department of Atmospheric Science, Colorado State University, Fort Collins, Colorado

(Manuscript received 25 May 2000, in final form 23 January 2001)

ABSTRACT

Equilibrium states of initially barotropically unstable polar vortices are predicted using two different approaches: minimum enstrophy and maximum entropy theories, which have been extended to include flows evolving on the surface of a sphere.

Minimum enstrophy theory shows very good agreement with an ensemble of direct numerical integrations of a polar vortex that mixes vorticity mainly on a spherical cap. For the case of a polar vortex with a substantial resistance to vorticity mixing at its core, the maximum entropy prediction shows good consistency with an ensemble of direct numerical integrations.

Maximum entropy theory gives an additional source of information with its density functions, which in a probabilistic sense reveal how the vorticity field (and therefore the mass field) is redistributed in the equilibrium state. The density functions show good skill in predicting several passive tracer distributions in the numerical experiments. Also, from a local point of view, density functions determine the degree of mixing of initially well separated air masses, information that is valuable in tracing atmospheric chemical components.

1. Introduction

The dynamic circulation of the stratosphere is strongly influenced by the seasonal cycle. In the summer hemisphere there is an easterly zonal-mean wind, while in the winter hemisphere the zonal-mean wind is westerly, with its most intense part comprising the ''polar night jet.'' The change from winter westerlies to summer easterlies occurs, on average, during March–April in the north and during October–November in the south. Bowman and Mangus (1993) presented Total Ozone Mapping Spectrometer (TOMS) sequences of images during the Southern Hemisphere spring. In their Fig. 1, the ozone hole is seen as a dark region centered over the South Pole, surrounded by a region of higher ozone values shown in white. Stretching and folding of the ozone field is observed to be qualitatively similar to the wave breaking of Ertel's potential vorticity (McIntyre and Palmer 1983, 1984). Another sequence of TOMS images (their Fig. 3) shows a typical breakdown of the polar vortex and the mixing of ozone over an extended region, with the consequent disappearance of the ozone hole. In this work we will study the evolution of a polar vortex with strong vorticity mixing at high latitudes and, in a different experiment, a polar vortex that maintains an isolated core, predicting their equilibrium states with two theories that are based upon the fundamental processes of high Reynolds number two-dimensional flows.

Numerical simulations of barotropic flows (e.g., McWilliams 1984; Yoden and Yamada 1993; Polvani et al. 1994; Cho and Polvani 1996), as well as laboratory experiments (e.g., Van de Konijnenberg et al. 1998) have shown the emergence of isolated coherent vortices from initial turbulent conditions. McWilliams (1984) modeled the decay of two-dimensional flow in a double-periodic square domain. An initially random condition on the vorticity field evolves in time to a collection of discrete and isolated vorticity extrema. The time series for the kinetic energy, enstrophy and the energy centroid wavenumber for this experiment showed a kinetic energy decay of about 3% over a time of 40 units, while the enstrophy decay was substantial (about 90%), although it slows considerably after $t = 10$. The energy centroid wavenumber decreases monotonically with time, which means that energy is transferred to larger scales, although its rate slows down with time.

Montgomery et al. (1992) performed a simulation with initial conditions as close as possible to those of McWilliams (1984), except that the duration of the run was approximately ten times longer. During the times of overlap, no significant differences were found. However, at long times the like-sign merger of vortices did not stop, but only slowed down. At the end of the simulation all possible like-sign vortex captures had oc-

Corresponding author address: Dr. Ricardo Prieto, Centro de Ciencias de la Atmósfera, UNAM, Circuito de la Investigación Científica, C.U., México 04510, D.F., Mexico.
E-mail: pricardo@atmosfera.unam.mx

curred, and only one vortex of each sign remained. This kind of phenomenon has been studied from different theoretical points of view, such as the selective decay hypothesis (Matthaeus and Montgomery 1980; Carnevale et al. 1991, 1992; Matthaeus et al. 1991) in which states of near minimal ratio of enstrophy to energy can be attained in short times compared with the decay time of the flow.

Making use of variational analysis Leith (1984) found two kinds of vortex structures, which represent the selective decay of enstrophy toward a minimum value, with the constraints of constant kinetic energy and angular momentum or circulation. Young (1987) applied the selective decay of enstrophy to a fluid in a periodic β-plane channel. Schubert et al. (1999) applied this ''minimum enstrophy'' idea to the redistribution of vorticity in hurricanes, thereby obtaining the minimum enstrophy radial profiles of vorticity, tangential wind, pressure and angular velocity, hypothesized as the end state of evolution for a hurricane after vorticity redistribution has taken place.

Onsager (1949) applied the standard methods of statistical mechanics to a system of point vortices in an incompressible frictionless fluid. This approach was extended to a collection of ''line'' vortices by Joyce and Montgomery (1973), and further developed by Miller (1990), Robert (1991), Robert and Sommeria (1991), and Sommeria et al. (1991). The idea behind this theory is to compute a local probability distribution of the vorticity field (''macroscopic'' or *coarse-grained* view), which describes the average ''microscopic'' or ''fine-grain'' fluctuations of the vorticity. One basic hypothesis is that the macroscopic equilibrium state, which is observed the most often, is the state for which the number of distributions of the microscopic vorticity field is a maximum. The most probable macroscopic state is the final equilibrium state of the flow. To find the most probable macroscopic state, we must find the particular probability distribution of vorticity that maximizes the functional known as the ''Boltzmann mixing entropy,'' subject to the integral constraints associated with the vorticity dynamics (such as the conservation of the kinetic energy, circulation and angular momentum); hence the name ''maximum entropy flows.''

For actual calculations using maximum entropy theory, we require some kind of discretization of the vorticity field. We will consider a two-dimensional fluid flow that consists of an array of vorticity patches. For fluids that consist of a large number of vorticity patches, the macroscopic state that maximizes the mixing entropy will be present an overwhelming number of times compared with the rest of macroscopic states and, therefore, will have the highest probability of being the one observed.

Robert and Sommeria (1991) proposed to apply the predictions of maximum entropy theory to geophysical problems, in particular to the atmosphere. In the present work, both minimum enstrophy theory and maximum entropy theory are applied to the stratospheric polar vortex.

2. Barotropic nondivergent model

When we consider motion that is horizontally nondivergent and barotropic, the governing equations of atmospheric flow reduce to the vorticity equation, which states the material conservation of absolute vorticity:

$$\frac{D\zeta}{Dt} = 0, \tag{2.1}$$

where

$$\frac{D}{Dt} \equiv \frac{\partial}{\partial t} + u\frac{\partial}{a\cos\phi\partial\lambda} + v\frac{\partial}{a\partial\phi} \tag{2.2}$$

is the material derivative, and

$$\zeta = 2\Omega\sin\phi + \frac{\partial v}{a\cos\phi\partial\lambda} - \frac{\partial(u\cos\phi)}{a\cos\phi\partial\phi} \tag{2.3}$$

is the absolute vorticity, with u and v the eastward and northward components of the velocity, λ the longitude, ϕ the latitude, t the time, a the radius of the earth, and Ω the angular rotation rate of the earth. Thus, under barotropic nondivergent conditions, the absolute vorticity behaves as a tracer of horizontal air motion and is rearranged by the circulation. On large scales, the actual atmospheric circulation tends to remain close to barotropic, which makes absolute vorticity approximately conserved.

The horizontal velocity field can be computed from the streamfunction ψ by

$$u = -\frac{\partial\psi}{a\partial\phi}, \qquad v = \frac{\partial\psi}{a\cos\phi\partial\lambda}, \tag{2.4}$$

and, as a result, the prognostic variable ζ can be expressed as a function of ψ by substituing (2.4) into (2.3) to obtain

$$\zeta = 2\Omega\sin\phi + \nabla^2\psi, \tag{2.5}$$

where ∇^2 is the two-dimensional Laplacian operator. With suitable initial conditions, the barotropic nondivergent vorticity equation (2.1) can be integrated for the motion at a later time.

The nonlinear system (2.1), (2.4), and (2.5) will be solved using the spherical harmonic spectral method in space, with explicit time differencing. The basic idea behind this method is to locally evaluate all nonlinear terms in physical space on an associated grid, also known as the transform grid. These terms are then transformed to wavenumber space to calculate linear terms and derivatives, and to obtain tendencies for the time-dependent variable. The computer code for this model was derived from the shallow water model of Hack and Jacob (1992). The method basically consists of representing a scalar variable like ζ as a truncated series of spherical harmonic functions $\zeta(\lambda, \mu) = \sum_{m=-M}^{M}$

$\Sigma_{n=|m|}^{N} \zeta_n^m P_n^m(\mu)e^{im\lambda}$, where $\mu \equiv \sin\phi$, M is the highest Fourier wavenumber included in the east–west representation and N is the highest degree of the associated Legendre functions included in the north–south representation. In this work, triangular truncation is used, meaning that $M \equiv N$. The nonlinear numerical model used here also includes the hyperdiffusion term $-\nu(\nabla^4\zeta - 4a^{-4}\zeta)$, which is added to the right-hand side of (2.1), to control accumulations in the smallest scales resolved by the numerical model. This type of diffusion results in significantly weaker damping on the resolved scales than $\nabla^2\zeta$ diffusion. The conservation of angular momentum requires inclusion of the term of $4a^{-4}\nu\zeta$. Thus, we expect the angular momentum to be a ''rugged invariant'' in the numerical simulations presented here.

Three integral properties associated with the $-\nu(\nabla^4 - 4a^{-4})\zeta$ diffusion are the angular momentum, energy, and enstrophy relations

$$\frac{d\mathcal{M}}{dt} = 0, \tag{2.6}$$

$$\frac{d\mathcal{E}}{dt} = -2\nu(4a^{-4}\mathcal{E} - \mathcal{P}), \tag{2.7}$$

$$\frac{d\mathcal{Z}}{dt} = -2\nu(\mathcal{L} - 4a^{-4}\mathcal{Z}), \tag{2.8}$$

where $\mathcal{M} = a^2 \int_{-1}^{1}\int_{0}^{2\pi} \mu\zeta \, d\lambda \, d\mu$ is the angular momentum, $\mathcal{E} = \int_{-1}^{1}\int_{0}^{2\pi} 1/2\nabla\psi\cdot\nabla\psi \, d\lambda \, d\mu$ is the kinetic energy, $\mathcal{Z} = \int_{-1}^{1}\int_{0}^{2\pi} 1/2\zeta^2 \, d\lambda \, d\mu$ is the absolute enstrophy, $\mathcal{P} = \int_{-1}^{1}\int_{0}^{2\pi} 1/2\nabla\zeta\cdot\nabla\zeta \, d\lambda \, d\mu$ is the palinstrophy, and $\mathcal{L} = \int_{-1}^{1}\int_{0}^{2\pi} 1/2(\nabla^2\zeta)^2 \, d\lambda \, d\mu$; these integral relations are easily obtained by multiplying the barotropic vorticity equation, with the hyperdiffusion term included, by μ, ψ, and ζ, respectively, and then integrating over the surface of the sphere. In the absence of dissipation, $\mathcal{E}$ and $\mathcal{Z}$ are strict invariants of the flow. With dissipation, $\mathcal{E}$ and $\mathcal{Z}$ are not strict invariants, but for the high Reynolds number flows we are considering, the kinetic energy $\mathcal{E}$ tends to be essentially invariant (i.e., rugged) while the enstrophy $\mathcal{Z}$ selectively decays.

The model also includes the computation of air parcel trajectories, which are of interest as tracers of materially conserved quantities, and in the quantitative estimation of atmospheric mixing. The trajectories are ''passive'' in the sense that the parcels are advected by the flow field, without having any feedback on the evolution of the flow field. At every time step, the model computes the new position of each of the initially defined air parcels, which total 1000.

3. Theory of minimum enstrophy flows on the sphere

Using the spherical harmonic expansion for the absolute vorticity and the orthogonality relations for the spherical harmonics, we can express (2.8) as

$$\frac{d\mathcal{Z}}{dt} = -\nu \int_{-1}^{1}\int_{0}^{2\pi} \sum_{m=-M}^{M}\sum_{n=|m|}^{N} \left[\left(\frac{n(n+1)}{a^2}\right)^2 - \frac{4}{a^4}\right](\mathrm{Re}[\zeta_n^m Y_n^m(\lambda,\mu)])^2 \, d\lambda \, d\mu. \tag{3.1}$$

Since the integrated vorticity is zero, $\zeta_0^0 = 0$. Then the integrand in (3.1) is always non-negative and if $\nu > 0$, then $d\mathcal{Z}/dt < 0$. Therefore, in our numerical simulations we expect that enstrophy is a decaying function of time due to hyperviscous dissipation.

Fjørtoft (1953) used the spherical harmonic expansion to compute the energy spectrum $\mathcal{E}(n, t)$ which is interpreted as the kinetic energy per unit mass per unit wavenumber. The enstrophy spectrum is given by $\mathcal{Z}(n, t) = a^{-2}n(n+1)\mathcal{E}(n, t)$. Fjørtoft (1953) showed that the energy fluxes towards low wavenumbers, while because of the $a^{-2}n(n+1)$ term, enstrophy fluxes towards high wavenumbers (small scales). Physically, this can be interpreted as the formation of large eddies while vorticity is sheared out as filaments. The factor $a^{-2}n(n+1)$ forces the enstrophy spectrum to peak at higher n, so that the effect of dissipation is greater on $\mathcal{Z}$ than on $\mathcal{E}$.

Merilees and Warn (1975) showed that in two-dimensional nondivergent flow on the plane and in a bounded region, roughly 70% of triad interactions lead to a larger energy exchange with lower wavenumbers, while about 60% exchange more enstrophy with higher wavenumbers. Extending that calculation to spherical geometry, Merilees and Warn (1975) estimated that, at the limit of large zonal wavenumber m, about 75% of interactions imply larger energy exchange with lower wavenumbers, and 55% exchange more enstrophy with higher wavenumbers; as m grows larger, those numbers converge to 70% and 60%, respectively.

This enstrophy cascade toward large wavenumbers and energy inverse cascade toward small wavenumbers has motivated the hypothesis of selective decay, used by Bretherton and Haidvogel (1976), Matthaeus and Montgomery (1980), Leith (1984), Young (1987), and Schubert et al. (1999). This hypothesis can be summarized as follows: The simplest state to which the flow might tend is that of minimum enstrophy compatible with the initial energy and/or other relevant constraints of the flow (like angular momentum).

Next, we develop the minimum enstrophy theory applied to flows on the sphere with one constraint, either angular momentum or energy. Let $\mu_e \equiv \sin\phi_e$ denote

the outer edge of the vorticity mixing region. Following Leith (1984) we first hypothesize that, out of the family of zonal flows that have the same integrated angular momentum north of $\mu = \mu_e$ and the same zonal wind at each latitude south of $\mu = \mu_e$, the zonal flow with minimum integrated enstrophy north of $\mu = \mu_e$ is the one toward which the flow actually evolves. This zonal flow is derived in section 3a and is called MinEF-$\mathcal{M}$, that is, the minimum enstrophy flow with constrained angular momentum. A modified version of MinEF-$\mathcal{M}$ where the vorticity mixing is confined within a latitude band, the ''two-edge problem,'' is derived in appendix A. As a second hypothesis we argue that, out of the family of zonal flows that have the same integrated energy north of $\mu = \mu_e$ and the same zonal wind at each latitude south of $\mu = \mu_e$, the flow with minimum integrated enstrophy north of $\mu = \mu_e$ is the one toward which the flow actually evolves. This vortex is called MinEF-$\mathcal{E}$, that is, the minimum enstrophy flow with constrained energy, and is presented in section 3b; the MinEF-$\mathcal{E}$ with two edges is derived in appendix B. Even when the predictions of minimum enstrophy theory presented in sections 3a,b and in appendixes A,B are local, that is, from one southern edge to the North Pole, or within a latitude band, the edge(s) of vorticity mixing is (are) not prescribed, and the model is allowed to compute it (them), giving a prediction of the extent of vorticity mixing.

a. Minimum enstrophy flow with fixed angular momentum and one edge (MinEF-$\mathcal{M}$)

Let us assume that vorticity mixing is confined to the north polar cap with unknown south edge μ_s. In the region $-1 \le \mu \le \mu_s$, the final zonally symmetric flow $U(\mu) \equiv u(\mu)\cos\phi$ is equal to the initial zonally symmetric flow $U_0(\mu)$ and the final absolute vorticity $\zeta(\mu)$ is equal to the initial absolute vorticity $\zeta_0(\mu)$. Requiring $U(\mu)$ to be a continuous function, we have

$$U(\mu_s) = U_0(\mu_s) \tag{3.2}$$

as the boundary condition on the final flow in the mixed region.

Given the conservation of total angular momentum, it is easy to show that maximizing the absolute enstrophy deficit is equivalent to maximizing the relative enstrophy deficit, that is: $\int_{\mu_s}^{1} 1/2(\zeta_0^2 - \zeta^2)\, d\mu = \int_{\mu_s}^{1} 1/2(\zeta_{r0}^2 - \zeta_r^2)\, d\mu$. We will consider the first alternative (i.e., maximize the absolute enstrophy deficit) for the calculations in this section.

We now explore the hypothesis that the final flow can be found by maximizing the enstrophy deficit (relative to the initial enstrophy) subject to the constraint of angular momentum invariance; that is,

$$\text{maximize} \quad \int_{\mu_s}^{1} \frac{1}{2}(\zeta_0^2 - \zeta^2)\, d\mu, \tag{3.3}$$

subject to

$$\int_{\mu_s}^{1} (U_0 - U)\, d\mu = 0. \tag{3.4}$$

To solve this problem we now vary the mixing edge μ_s, the zonal wind profile $U(\mu)$, and the associated vorticity profile $\zeta(\mu)$ in search of that zonal flow that has maximum enstrophy deficit (i.e., minimum enstrophy) for fixed angular momentum. Since μ_s is unknown, its first variation is related to the first variation in U at that latitude by $\delta U(\mu_s) = [U_0'(\mu_s) - U'(\mu_s)]\delta\mu_s = -a[\zeta_0(\mu_s) - \zeta(\mu_s)]\delta\mu_s$ (e.g., Fox 1987, 210–213). Using this result, introducing the Lagrange multiplier $-\gamma$, and recalling Leibniz's rule, the variational problem is

$$\begin{aligned}
0 &= \delta \int_{\mu_s}^{1} \left[\frac{1}{2}(\zeta_0^2 - \zeta^2) - \gamma(U_0 - U)\right] d\mu \\
&= \int_{\mu_s}^{1} (-\zeta\delta\zeta + \gamma\delta U)\, d\mu - \frac{1}{2}[\zeta_0^2(\mu_s) - \zeta^2(\mu_s)]\delta\mu_s \\
&= \int_{\mu_s}^{1} \left(-\frac{d\zeta}{a d\mu} + \gamma\right)\delta U\, d\mu - \frac{1}{a}\zeta(\mu_s)\delta U(\mu_s) \\
&\quad - \frac{1}{2}[\zeta_0^2(\mu_s) - \zeta^2(\mu_s)]\delta\mu_s \\
&= \int_{\mu_s}^{1} \left(-\frac{d\zeta}{a d\mu} + \gamma\right)\delta U\, d\mu - \frac{1}{2}[\zeta_0(\mu_s) - \zeta(\mu_s)]^2\delta\mu_s,
\end{aligned} \tag{3.5}$$

where the third line follows from an integration by parts, along with the relation $a\delta\zeta = -d(\delta U)/d\mu$. For the independent variation $\delta\mu_s$, we obtain the transversality condition

$$\zeta(\mu_s) = \zeta_0(\mu_s). \tag{3.6}$$

For the independent variation δU, we obtain the Euler–Lagrange equation

$$\frac{d\zeta}{a d\mu} = \gamma \quad \text{for } \mu_s \le \mu \le 1. \tag{3.7}$$

We can obtain the solutions for $\zeta(\mu)$ and $U(\mu)$ by first integrating (3.7) and enforcing the transversality condition (3.6), and then integrating $d[U + \Omega a(1 - \mu^2)]/d\mu = -a\zeta$ and enforcing the boundary condition (3.2) and the condition $U(1) = 0$. We thus obtain

$$\begin{aligned}
\zeta(\mu) &= \zeta_0(\mu_s) + 2\left[\frac{U_0(\mu_s) + \Omega a(1 - \mu_s^2)}{a(1 - \mu_s)} - \zeta_0(\mu_s)\right] \\
&\quad \times \left(\frac{\mu - \mu_s}{1 - \mu_s}\right),
\end{aligned} \tag{3.8}$$

$$\begin{aligned}
U(\mu) &+ \Omega a(1 - \mu^2) \\
&= [U_0(\mu_s) + \Omega a(1 - \mu_s^2) - a\zeta_0(\mu_s)(1 - \mu_s)] \\
&\quad \times \left[1 - \left(\frac{\mu - \mu_s}{1 - \mu_s}\right)^2\right] + a\zeta_0(\mu_s)(1 - \mu),
\end{aligned} \tag{3.9}$$

for $\mu_s \le \mu \le 1$. Note that (3.9) satisfies the boundary condition (3.2). For given initial conditions $U_0(\mu)$ and $\zeta_0(\mu)$, the transcendental relation for the determination of the mixing edge μ_s is obtained by substituting (3.9) into the angular momentum constraint (3.4). We can now summarize the argument for MinEF-$\mathcal{M}$: Given an initial unstable zonally symmetric flow with zonal wind $U_0(\mu)$ and vorticity $\zeta_0(\mu)$, first determine μ_s from (3.4) and (3.9). The final adjusted vorticity profile $\zeta(\mu)$ and zonal wind profile $U(\mu)$ are then given by (3.8) and (3.9).

In appendix A we develop the minimum enstrophy theory for flows with fixed angular momentum and two edges.

b. Minimum enstrophy flow with fixed energy and one edge (MinEF-$\mathcal{E}$)

We assume that, in the region $-1 \le \mu \le \mu_s$, the final angular velocity $\omega(\mu) \equiv a^{-1}u(\mu)(1-\mu^2)^{-1/2}$ is equal to the initial angular velocity $\omega_0(\mu)$, so that in particular

$$\omega(\mu_s) = \omega_0(\mu_s). \tag{3.10}$$

We now explore the hypothesis that the final flow can be found by maximizing the enstrophy deficit subject to the constraint of kinetic energy invariance; that is,

$$\text{maximize} \quad \int_{\mu_s}^{1} \frac{1}{2}(\zeta_0^2 - \zeta^2)\, d\mu, \tag{3.11}$$

subject to

$$\int_{\mu_s}^{1} \frac{1}{2}(u_0^2 - u^2)\, d\mu = 0. \tag{3.12}$$

We now vary μ_s, the zonal wind profile $u(\mu)$, and the associated vorticity profile $\zeta(\mu)$ in search of that zonal flow that has maximum enstrophy deficit for fixed energy. Introducing the Lagrange multiplier β, the variational problem is

$$\begin{aligned}
0 &= \delta \int_{\mu_s}^{1} \frac{1}{2}[\zeta_0^2 - \zeta^2 + \beta(u_0^2 - u^2)]\, d\mu \\
&= -\int_{\mu_s}^{1} (\zeta\delta\zeta + \beta u\delta u)\, d\mu - \frac{1}{2}[\zeta_0^2(\mu_s) - \zeta^2(\mu_s)]\delta\mu_s \\
&= -\int_{\mu_s}^{1} (\zeta - \beta\psi)\delta\zeta\, d\mu - \frac{\beta}{a}\psi(\mu_s)\delta U(\mu_s) \\
&\quad - \frac{1}{2}[\zeta_0^2(\mu_s) - \zeta^2(\mu_s)]\delta\mu_s \\
&= -\int_{\mu_s}^{1} (\zeta - \beta\psi)\delta\zeta\, d\mu \\
&\quad - \frac{1}{2}[\zeta_0(\mu_s) + \zeta(\mu_s) - 2\beta\psi(\mu_s)] \\
&\quad \times [\zeta_0(\mu_s) - \zeta(\mu_s)]\delta\mu_s,
\end{aligned} \tag{3.13}$$

where the third line of (3.13) results from an integration by parts. For the independent variation $\delta\mu_s$, we again obtain the transversality condition

$$\zeta(\mu_s) = \zeta_0(\mu_s). \tag{3.14}$$

For the independent variation $\delta\zeta$, we obtain $\zeta = -a^{-2}\alpha(\alpha+1)\psi$ for $\mu_s \le \mu \le 1$, where α is defined in terms of the Lagrange multiplier by $\alpha(\alpha+1) = -\beta a^2$. When written in terms of the streamfunction, this linear relation between ζ and ψ takes the form

$$\begin{aligned}
(1-\mu^2)\frac{d^2\psi}{d\mu^2} - 2\mu\frac{d\psi}{d\mu} + \alpha(\alpha+1)\psi \\
= -2\Omega a^2\mu \quad \text{for } \mu_s \le \mu \le 1.
\end{aligned} \tag{3.15}$$

The general solution of (3.15) is $\psi(\mu) = AP_\alpha(\mu) + BQ_\alpha(\mu) + 2\Omega a^2\mu/[2 - \alpha(\alpha+1)]$, where $P_\alpha(\mu)$ and $Q_\alpha(\mu)$ are the Legendre functions of (noninteger) order α, and A and B are constants. The Legendre function $P_\alpha(\mu)$ is not finite at $\mu = -1$ while the Legendre function $Q_\alpha(\mu)$ is not finite at $\mu = 1$. Since we are considering mixing in the north polar cap, we set $B = 0$. Since $\zeta(\mu) = -a^{-2}\alpha(\alpha+1)\psi$, the solution for the vorticity is $\zeta(\mu) = -a^{-2}\alpha(\alpha+1)\{AP_\alpha(\mu) + 2\Omega a^2\mu/[2 - \alpha(\alpha+1)]\}$. The constant A can now be obtained by enforcing the transversality condition (3.14). This results in

$$\begin{aligned}
\zeta(\mu) = \left[\zeta_0(\mu_s) - \left(\frac{\alpha(\alpha+1)2\Omega\mu_s}{\alpha(\alpha+1) - 2}\right)\right]\frac{P_\alpha(\mu)}{P_\alpha(\mu_s)} \\
+ \frac{\alpha(\alpha+1)2\Omega\mu}{\alpha(\alpha+1) - 2}
\end{aligned} \tag{3.16}$$

for $\mu_s \le \mu \le 1$. Since the angular velocity is related to the streamfunction by $\omega(\mu) = -a^{-2}(d\psi/d\mu)$, we can also determine the constant A by enforcing (3.10). This results in

$$\begin{aligned}
\omega(\mu) = \left[\omega_0(\mu_s) - \frac{2\Omega}{\alpha(\alpha+1) - 2}\right]\frac{P'_\alpha(\mu)}{P'_\alpha(\mu_s)} \\
+ \frac{2\Omega}{\alpha(\alpha+1) - 2},
\end{aligned} \tag{3.17}$$

where primed quantities represent derivatives with respect to μ. Because $\zeta(\mu)$ and $\omega(\mu)$ are related by $\zeta = 2\Omega\mu - d[(1-\mu^2)\omega]/d\mu$, consistency between (3.16) and (3.17) requires

$$\begin{aligned}
\alpha(\alpha+1)\left[\omega_0(\mu_s) - \frac{2\Omega}{\alpha(\alpha+1) - 2}\right]P_\alpha(\mu_s) \\
= \left[\zeta_0(\mu_s) - \frac{\alpha(\alpha+1)2\Omega\mu_s}{\alpha(\alpha+1) - 2}\right]P'_\alpha(\mu_s).
\end{aligned} \tag{3.18}$$

For given initial conditions $\omega_0(\mu)$ and $\zeta_0(\mu)$, (3.18) constitutes one of the two transcendental relations required for the determination of the mixing edge μ_s and the

Lagrange multiplier α. The other relation is obtained by substituting (3.17) into the energy constraint (3.12). We can summarize the MinEF-$\mathcal{E}$ argument as follows. Given an initial unstable zonal flow with angular velocity $\omega_0(\mu)$ and vorticity $\zeta_0(\mu)$, first determine α, and μ_s from (3.12) and (3.18). The final adjusted vorticity profile $\zeta(\mu)$ and angular velocity profile $\omega(\mu)$ are then given by (3.16) and (3.17).

In appendix B we explain the theory of minimum enstrophy flow with fixed energy and two edges.

4. Theory of maximum entropy flows on the sphere

Direct numerical integrations like those presented in Legras and Dritschel (1993), Ishioka and Yoden (1994), Norton (1994), and Waugh and Plumb (1994) illustrate how barotropic instability processes can produce intricate vorticity patterns. An alternative approach for predicting ''end states'' has recently been developed by Miller (1990), Robert (1991), Robert and Sommeria (1991, 1992), Sommeria et al. (1991), Miller et al. (1992), Whitaker and Turkington (1994), Chavanis and Sommeria (1996, 1998), and Turkington and Whitaker (1996), but their basic ideas date back to the origins of the kinetic theory of gases and statistical mechanics. The general nature of the statistical mechanical procedure for the treatment of complicated systems involves abandoning the attempt to follow the precise changes in state that would take place in a particular system, and studying instead the behaviour of a collection or ensemble of systems of similar structure to the system of actual interest. From a knowledge of the average behaviour of the systems in a representative ensemble, appropriately chosen so as to correspond to the partial knowledge that we do have as to the initial state of the system of interest, we can then make predictions as to what may be expected, on the average, for the particular system that concerns us.

For the specific case of interest here, the specification of the initial values of the total energy, angular momentum and circulation, defines a particular macroscopic state of the system. However, at the ''microscopic'' level, there exist a large number of vorticity fields that are consistent with the macroscopic state. Each of the different vorticity fields specifies a particular ''microstate.'' To a given macrostate there corresponds a large number of microstates (vorticity fields), and it seems natural to assume that at any time t the system is equally likely to be in any of these microstates. The numerical method that is described in this section has the purpose of finding the macrostate that has the largest number of microstates, consistent with the knowledge we have of the state of the system (i.e., its energy, angular momentum, and circulation). The basic hypothesis is that the most probable macroscopic state is the final equilibrium state of the flow. It should be emphasized that this method has a statistical character, and that the results that it provides are not necessarily precisely true in an individual case, but are true in an average sense for the systems in an appropriately chosen ensemble.

Numerical method

Here we present a simple version of the maximum entropy argument. In particular, from the definition of the absolute vorticity by equation (2.3), we assume that the initial state consists of L levels of absolute vorticity $\hat{\zeta}_l$ with fractional area $\mathcal{A}_l$, $l = 1, \ldots, L$. These initial parameters are not all independent, but must satisfy $\Sigma_{l=1}^{L} \mathcal{A}_l = 1$ and $\Sigma_{l=1}^{L} \hat{\zeta}_l \mathcal{A}_l = 0$ (since the absolute vorticity integrated over the sphere must vanish). Denoting the initial absolute vorticity by $\zeta_0(\lambda, \mu)$ and the initial streamfunction by $\psi_0(\lambda, \mu)$, we note that $\nabla^2 \psi_0 = \zeta_0 - 2\Omega\mu$ on the spherical domain. The solution of this Poisson problem on the spherical domain is only unique to within an arbitrary additive constant. We fix this constant by requiring that $\int_{-1}^{1} \int_{0}^{2\pi} \psi_0(\lambda, \mu)\, d\lambda\, d\mu = 0$. We make a similar argument for the final streamfunction $\psi(\lambda, \mu)$, and hence require $\int_{-1}^{1} \int_{0}^{2\pi} \psi(\lambda, \mu)\, d\lambda\, d\mu = 0$.

To begin the argument let us suppose that, after the absolute vorticity field has become intricately stretched and folded, we sample it at N points within a small neighborhood of λ, μ. Let n_l denote the number of sampled points at which the absolute vorticity value $\hat{\zeta}_l$ is found. Then $\rho_l(\lambda, \mu) = n_l/N$ denotes the probability, at point (λ, μ), of finding the absolute vorticity $\hat{\zeta}_l$, and the macroscopic absolute vorticity at point (λ, μ) is

$$\zeta(\lambda, \mu) = \sum_{l=1}^{L} \hat{\zeta}_l \rho_l(\lambda, \mu). \tag{4.1}$$

From the statistical mechanics view, the macroscopic equilibrium state is that which has a maximum number of distributions of the sampled points which are consistent with the absolute vorticity field $\zeta(\lambda, \mu)$, in other words, the most mixed state. Therefore we must count the total number W of corresponding distributions. The number of possible arrangements having n_1 points with absolute vorticity $\hat{\zeta}_1$, n_2 points with absolute vorticity $\hat{\zeta}_2$, etc., is the multiplicity function W, which is given by

$$W = \frac{N!}{n_1! n_2! \cdots n_L!}. \tag{4.2}$$

The division by $n_1! n_2! \cdots n_L!$ comes from the fact that two sampled points of vorticity with the same vorticity value are indistinguishable if their positions are interchanged. The logarithm of the multiplicity function is $\ln W = \ln N! - \Sigma_{l=1}^{L} \ln n_l!$. Using the Stirling approximation (e.g., $\ln N! \approx N \ln N - N$ for large N), we obtain $\ln W \approx N \ln N - \Sigma_{l=1}^{L} n_l \ln n_l = -\Sigma_{l=1}^{L} n_l \ln(n_l/N)$, where we have used $\Sigma_{l=1}^{L} n_l = N$. We conclude that

$$\lim_{N \to \infty} \left(\frac{1}{N} \ln W \right) = -\sum_{l=1}^{L} \rho_l \ln \rho_l. \tag{4.3}$$

We now define the Boltzmann mixing entropy $S[\rho_1(\lambda, \mu), \ldots, \rho_L(\lambda, \mu)]$ as

$$S[\rho_1(\lambda, \mu), \ldots, \rho_L(\lambda, \mu)] = \int_{-1}^{1}\int_{0}^{2\pi}\left(-\sum_{l=1}^{L}\rho_l(\lambda, \mu)\ln\rho_l(\lambda, \mu)\right)d\lambda\, d\mu. \quad (4.4)$$

The functional $S[\rho_1(\lambda, \mu), \ldots, \rho_L(\lambda, \mu)]$ measures the loss of information in going from the *fine-grain* (microscopic) view to the *coarse-grain* (macroscopic) view. To find the most probable macroscopic state, we must find the particular set of functions $\rho_l(\lambda, \mu)$, $l = 1, \ldots, L$, which maximize $S[\rho_1(\lambda, \mu), \ldots, \rho_L(\lambda, \mu)]$ subject to all the integral constraints associated with the inviscid vorticity dynamics. The kinetic energy constraint requires that the final and initial kinetic energies be equal; that is, $\int_{-1}^{1}\int_{0}^{2\pi} 1/2(u^2 + v^2)\, d\lambda\, d\mu = \int_{-1}^{1}\int_{0}^{2\pi} 1/2(u_0^2 + v_0^2)\, d\lambda\, d\mu$, where the subscript zero denotes the initial state. With the aid of $(u, v\cos\phi) = (-\partial\psi/a\partial\phi, \partial\psi/a\partial\lambda)$ and $(u_0, v_0\cos\phi) = (-\partial\psi_0/a\partial\phi, \partial\psi_0/a\partial\lambda)$, we can use integration by parts to express the kinetic energy constraint as $\int_{-1}^{1}\int_{0}^{2\pi}\psi\zeta_r\, d\lambda\, d\mu = \int_{-1}^{1}\int_{0}^{2\pi}\psi_0\zeta_{r0}\, d\lambda\, d\mu$, where ζ_r is the relative vorticity. The angular momentum constraint requires that the final and initial angular momenta be equal; that is, $\int_{-1}^{1}\int_{0}^{2\pi} m\, d\lambda\, d\mu = \int_{-1}^{1}\int_{0}^{2\pi} m_0\, d\lambda\, d\mu$, where $m = (u + \Omega a\cos\phi)a\cos\phi$ is the absolute angular momentum per unit mass. With the aid of (2.3) we can use integration by parts to express the angular momentum constraint as $\int_{-1}^{1}\int_{0}^{2\pi}\mu\zeta\, d\lambda\, d\mu = \int_{-1}^{1}\int_{0}^{2\pi}\mu\zeta_0\, d\lambda\, d\mu$. In other words, the variational problem is to find the expectation functions $\rho_l(\lambda, \mu)$ by maximizing (4.4) subject to the circulation constraints

$$\int_{-1}^{1}\int_{0}^{2\pi}\rho_l(\lambda, \mu)\, d\lambda\, d\mu = 4\pi\mathcal{A}_l, \qquad l = 1, 2, \ldots, L, \quad (4.5)$$

the angular momentum constraint

$$\int_{-1}^{1}\int_{0}^{2\pi}\mu\left(\sum_{l=1}^{L}\hat{\zeta}_l\rho_l\right)d\lambda\, d\mu = \int_{-1}^{1}\int_{0}^{2\pi}\mu\zeta_0\, d\lambda\, d\mu, \quad (4.6)$$

and a combination of the energy constraint and the angular momentum constraint

$$\int_{-1}^{1}\int_{0}^{2\pi}\psi\left(\sum_{l=1}^{L}\hat{\zeta}_l\rho_l\right)d\lambda\, d\mu = \int_{-1}^{1}\int_{0}^{2\pi}\psi_0\zeta_0\, d\lambda\, d\mu. \quad (4.7)$$

In the last two relations (4.1) has been used. Making use of standard techniques of the calculus of variations, we take a linear combination of (4.4)–(4.7) in the following manner. Multiply (4.4) by unity, (4.5) by α_l, (4.7) by $1/2\beta$, and (4.6) by γ; then add, and take the variation of the resulting equation:

$$\begin{aligned} 0 &= \delta\int_{-1}^{1}\int_{0}^{2\pi}\sum_{l=1}^{L}\left[-\rho_l\ln\rho_l + \alpha_l\rho_l + \hat{\zeta}_l\left(\frac{1}{2}\beta\psi + \gamma\mu\right)\rho_l\right]d\lambda\, d\mu \\ &= \int_{-1}^{1}\int_{0}^{2\pi}\sum_{l=1}^{L}\left\{(-1 - \ln\rho_l)\delta\rho_l + \alpha_l\delta\rho_l + \hat{\zeta}_l\left[\frac{1}{2}\beta(\psi\delta\rho_l + \rho_l\delta\psi) + \gamma\mu\delta\rho_l\right]\right\}d\lambda\, d\mu \\ &= \int_{-1}^{1}\int_{0}^{2\pi}\sum_{l=1}^{L}[-1 - \ln\rho_l + \alpha_l + \hat{\zeta}_l(\beta\psi + \gamma\mu)]\delta\rho_l\, d\lambda\, d\mu. \end{aligned} \quad (4.8)$$

The third line has been obtained using the integral over the spherical domain of the relation $\nabla\cdot[\psi\nabla\delta\psi - \delta\psi\nabla\psi] = \psi\delta\zeta - \zeta\delta\psi$, together with (4.1). The quantities α_l, β, and γ are Lagrange multipliers. For arbitrary variations $\delta\rho_l$ we obtain from (4.8)

$$1 + \ln\rho_l = \alpha_l + \hat{\zeta}_l(\beta\psi + \gamma\mu), \qquad l = 1, 2, \ldots, L. \quad (4.9)$$

Solving (4.9) for $\rho_l(\lambda, \mu)$ and requiring $\Sigma_{l=1}^{L}\rho_l = 1$, we obtain

$$\rho_l(\lambda, \mu) = \frac{1}{Z}\exp[\alpha_l + \hat{\zeta}_l(\beta\psi + \gamma\mu)], \quad (4.10)$$

where the partition function Z is given by

$$Z = \sum_{l=1}^{L}\exp[\alpha_l + \hat{\zeta}_l(\beta\psi + \gamma\mu)]. \quad (4.11)$$

Using (4.10) in (4.1), we obtain

$$\zeta = \frac{1}{Z}\sum_{l=1}^{L}\hat{\zeta}_l\exp[\alpha_l + \hat{\zeta}_l(\beta\psi + \gamma\mu)], \quad (4.12)$$

which can be used in the invertibility relation

$$\nabla^2\psi = \zeta - 2\Omega\mu \quad (4.13)$$

to obtain the streamfunction. Since the right-hand side of (4.13) depends on ψ through (4.12), we are faced with solving a nonlinear partial differential equation for $\psi(\lambda, \mu)$ with yet to be determined Lagrange multipliers

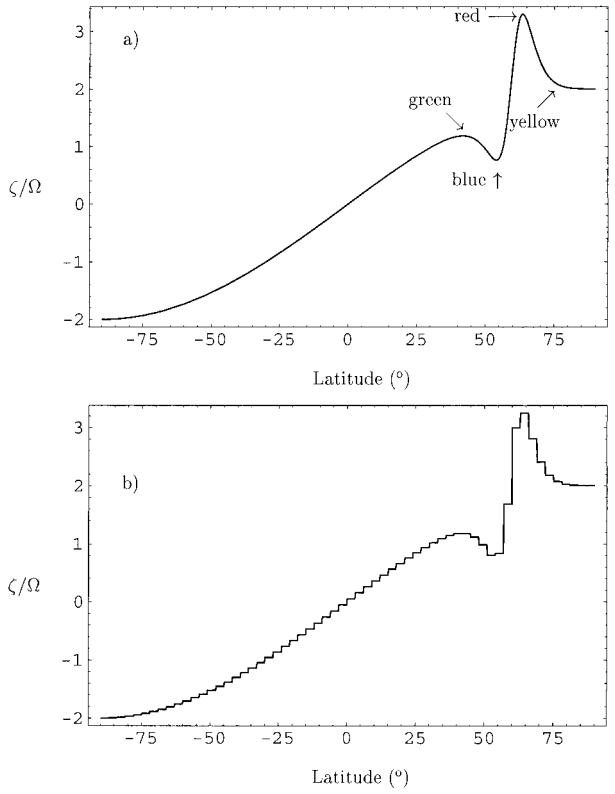

FIG. 1. Initial absolute vorticity profiles for experiment 1: (a) direct numerical integration and (b) maximum entropy theory. The arrows denote the initial positions of the colored tracers shown in Fig. 2.

α_l, β, γ. The equations for α_l, β, γ are obtained by enforcing the constraints (4.5)–(4.7). In summary, the solution of the maximum entropy flow problem involves solving the nonlinear system (4.5), (4.6), (4.7), (4.12), (4.13) for α_l, β,γ, $\zeta(\lambda, \mu)$, $\psi(\lambda, \mu)$, given the initial flow. Analytical solutions of this system are not easily obtained, and numerical methods are required.

Turkington and Whitaker (1996) have proposed an iterative algorithm based on the variational structure of the constrained optimization problem. The extension of this algorithm to spherical geometry generates the ν^{th} iterate $\alpha_l^{(\nu)}$, $\beta^{(\nu)}$, $\gamma^{(\nu)}$, $\rho_l^{(\nu)}(\lambda, \mu)$, $\zeta^{(\nu)}(\lambda, \mu)$, $\psi^{(\nu)}(\lambda, \mu)$ from $\zeta^{(\nu-1)}(\lambda, \mu)$, $\psi^{(\nu-1)}(\lambda, \mu)$ by maximizing $S[\rho_1^{(\nu)}(\lambda, \mu), \ldots, \rho_L^{(\nu)}(\lambda, \mu)]$, subject to the circulation, energy, and absolute angular momentum constraints. Given the initial condition, the iteration proceeds as follows: 1) Knowing $\zeta^{(\nu-1)}(\lambda, \mu)$ and $\psi^{(\nu-1)}(\lambda, \mu)$ from the previous iteration (or from an initial guess), solve $L + 1$ algebraic equations for $\alpha_l^{(\nu)}$, $\beta^{(\nu)}$, $\gamma^{(\nu)}$; 2) substitute the $\alpha_l^{(\nu)}$, $\beta^{(\nu)}$, $\gamma^{(\nu)}$ into (4.12) to obtain $\zeta^{(\nu)}(\lambda, \mu)$; and 3) knowing $\zeta^{(\nu)}(\lambda, \mu)$, solve the invertibility relation (4.13) for $\psi^{(\nu)}(\lambda, \mu)$, and return to step 1. As in Whitaker and Turkington (1994), the stopping criterion is chosen to be $|E^{(\nu)} - E^{(0)}|/|E^{(0)}| \leq 5 \times 10^{-3}$, where $E^{(0)} = -\int_{-1}^{1} \int_{0}^{2\pi} 1/2 \psi_0 \zeta_{r0}\, d\lambda\, d\mu$ and $E^{(\nu)} = -\int_{-1}^{1} \int_{0}^{2\pi} 1/2\, \psi^{(\nu)} \zeta_r^{(\nu)}\, d\lambda\, d\mu$. The number of iterations required for convergence varies depending on the initialization, but typically from ten to twenty iterations are sufficient to satisfy this stopping criterion.

5. Experiments

Suggestions that shear instabilities, either barotropic or baroclinic, might play a role in the behavior of the stratospheric polar vortex have been made since the 1960s, as summarized by McIntyre (1982). Hartmann (1983) argued that the continuous forcing of radiative processes in the stratosphere can create large positive zonal wind curvature and then small potential vorticity gradient. In Hartmann's (1983) Fig. 1b, the monthly mean cross section of the gradient of potential vorticity for the month of August 1979 in the Southern Hemisphere has regions of negative potential vorticity, suggesting the possibility that shear instability processes could alter the wind profile over time. Following Hartmann's (1983) work, we perform a set of direct numerical integrations to determine the equilibrium states of the stratospheric polar vortex, and then compare these results with the predictions given by the maximum entropy and minimum enstrophy theories.

As an initial condition to model the behavior of an unstable polar vortex we have selected two types of zonally symmetric jets. These profiles, used by Hartmann (1983) and Ishioka and Yoden (1994), are the sech-type jet

$$u_0(\phi) = U \cos\phi \operatorname{sech}\left[\frac{2(\phi - \phi_0)}{B}\right], \tag{5.1}$$

and the tanh-type jet

$$u_0(\phi) = \frac{U}{2} \cos\phi \left[1 + \tanh\left(\frac{\phi - \phi_0}{B}\right)\right], \tag{5.2}$$

where the constants U, ϕ_0, and B measure the strength, position, and width of the jet. In this section we will discuss the direct numerical integration and final equilibrium state of one experiment using the sech-type jet and one experiment using the tanh-type jet.

a. Experiment 1: Sech-type jet

Experiment 1 is the sech-type jet (5.1) with $U = 180$ m s^{-1}, $\phi_0 = 60°$N, and $B = 10°$, which is the experiment shown in Fig. 11a of Ishioka and Yoden (1994). The initial absolute vorticity is

$$\zeta_0(\phi) = \frac{2}{aB} u_0(\phi) \tanh\left[\frac{2(\phi - \phi_0)}{B}\right] + \frac{2u_0(\phi)}{a} \tan\phi + 2\Omega \sin\phi. \tag{5.3}$$

This initial condition has two regions where the absolute vorticity gradient is negative (see Fig. 1a) and thus satisfies Kuo's (1949) necessary condition for barotropic

TABLE 1. Definitions of the intial perturbations for the ensembles of direct numerical integrations of experiments 1 and 2. The disturbance vorticity $\zeta_d(\lambda, \phi; \lambda_d, \phi_d)$ is defined in (5.4).

Experiments	Initial perturbation
1A, 2A	$\zeta_d\left(\lambda, \phi; 0, \frac{\pi}{4}\right)$
1B, 2B	$\zeta_d\left(\lambda, \phi; 0, \frac{\pi}{4}\right) + \zeta_d\left(\lambda, \phi; \pi, \frac{\pi}{4}\right)$
1C, 2C	$\zeta_d\left(\lambda, \phi; 0, \frac{\pi}{4}\right) + \zeta_d\left(\lambda, \phi; \frac{\pi}{2}, \frac{\pi}{3}\right)$
1D, 2D	$\zeta_d\left(\lambda, \phi; 0, \frac{\pi}{4}\right) + \zeta_d\left(\lambda, \phi; \frac{2\pi}{3}, \frac{\pi}{4}\right) + \zeta_d\left(\lambda, \phi; \frac{4\pi}{3}, \frac{\pi}{4}\right)$
1E, 2E	$\zeta_d\left(\lambda, \phi; 0, \frac{\pi}{4}\right) + \zeta_d\left(\lambda, \phi; \frac{\pi}{2}, \frac{\pi}{4}\right) + \zeta_d\left(\lambda, \phi; \pi, \frac{\pi}{4}\right) + \zeta_d\left(\lambda, \phi; \frac{3\pi}{2}, \frac{\pi}{4}\right)$

instability. The global maximum of $\zeta_0(\phi)$ is at $\phi = 63.5°$N, with a local maximum at $\phi = 41.8°$N and two local minima at 54°N and at the North Pole. Figure 1b shows a discretized version of $\zeta_0(\phi)$ consisting of 60 vorticity levels to be used as initial condition for the maximum entropy prediction.

Ishioka and Yoden (1994) and Hartmann (1983) presented results of a linear stability analysis for the ''polar'' mode and for the ''midlatitude'' mode. Polar modes show instability for zonal wavenumbers 1 to 4, while midlatitude modes are unstable for zonal wavenumbers 2 to 7. The most unstable (midlatitude) mode is wavenumber 4 with an *e*-folding time of 1.1 days and a period of 1.7 days.

The nonlinear barotropic nondivergent model described in section 2 was used to study the evolution of the initial vorticity field given by (5.3). An ensemble of five experiments was run, with the only difference being the way instability was initiated. Table 1 defines the five perturbations for experiments A–E, where

$$\zeta_d(\lambda, \phi; \lambda_d, \phi_d) = c_1\left(e^{c_2(g(\lambda,\phi;\lambda_d,\phi_d)-1)} - \frac{1 - e^{-2c_2}}{2c_2}\right), \quad \text{and} \tag{5.4}$$

$$g(\lambda, \phi; \lambda_d, \phi_d) = \sin\phi \sin\phi_d + \cos\phi \cos\phi_d \cos(\lambda - \lambda_d). \tag{5.5}$$

Here $c_1 = 0.01\Omega$ and $c_2 = 100$, which are measures of the intensity and horizontal extent of the disturbance, respectively. The disturbance vorticity $\zeta_d(\lambda, \phi; \lambda_d, \phi_d)$ is identical to the one used by Ishioka and Yoden (1994). It is a smooth Gaussian-like function centered at (λ_d, ϕ_d), with nearly white spectra in wavenumber space for large c_2. The initial perturbations listed in Table 1 will also be used for the nonlinear integrations discussed in section 5b.

The nonlinear barotropic model uses a triangular truncation with $M = 150$, $\nu = 2.23 \times 10^{14}$ m^4 s^{-1}, and a time step of 300 s. Results for experiment 1A are shown in Fig. 2. The plots are polar stereographic projections of the absolute vorticity field, where the lowest latitude circle is 30°N and the North Pole is at the center of each diagram. Longitude $\lambda = 0$ corresponds to the straight line that runs from the North Pole downward on the page. The value of the hyperdiffusion coefficient ν was obtained empirically via a preliminary set of runs, and corresponds to a 1/*e* damping time of 4 h for the highest wavenumber ($n = 150$). We have included trajectory calculations for 1000 colored air parcels, initially distributed in 4 rings with 250 colored parcels each. The green ring is placed at the relative maximum of $\zeta_0(\phi)$ at $\phi = 41.8°$N; the blue ring is at the relative minimum of $\zeta_0(\phi)$ at $\phi = 54°$N; 250 red air parcels are at the maximum of absolute vorticity ($\phi = 63.5°$N) and a ring closer to the pole ($\phi = 75°$N) consists of 250 yellow air parcels.

After 6.0 days there clearly emerges a folding of absolute vorticity contours at latitudes close to the blue ring. At $t = 8.0$ days a zonal wavenumber 4 instability is seen at midlatitudes, equatorward of the highest absolute vorticity gradient, and another wavenumber 4 instability occurs poleward of the highest absolute vorticity gradient. At $t = 10.0$ days, strong mixing of vorticity is observed at middle and high latitudes. Green air parcels have been advected toward the polar vortex edge and blue air parcels toward lower latitudes. The yellow and red rings preserve most of their integrity while they move around the pole and begin to switch places. Long, thin filaments are observed both inside and outside the region of highest absolute vorticity gradient. From $t = 10$ days to $t = 25$ days strong mixing is observed, with detachment and diffusion of vorticity filaments, as well as dispersion of colored air parcels northward of 20°N. The state of the flow at $t = 30.0$ days (Fig. 2e) is more symmetric and the distribution of tracers is quite different with respect to the initial condition. At the end of the time integration (100 days), the polar vortex has returned to a zonally symmetric state, with colored air parcels distributed over the whole Northern Hemisphere. Comparing Figs. 2a–d and 2e,f, we can observe that most of the redistribution of the vorticity field and tracers took place between $t = 6$ days and $t = 30$ days, while the last 70 days of integration had a less important effect on the mixing of the flow.

Figure 3 shows the absolute vorticity field at $t = 10$ days for experiments 1B–E. The display of the tracers is omitted. Even though these experiments were all started from the same basic zonal flow field, it is clear that the initial perturbation has an important effect on the precise evolution of the flow.

The averaged histograms of tracer positions as a function of latitude at $t = 100$ days for the ensemble of experiments 1A–E are shown in Fig. 4. The counting is done within 5° latitude bands dividing by the total

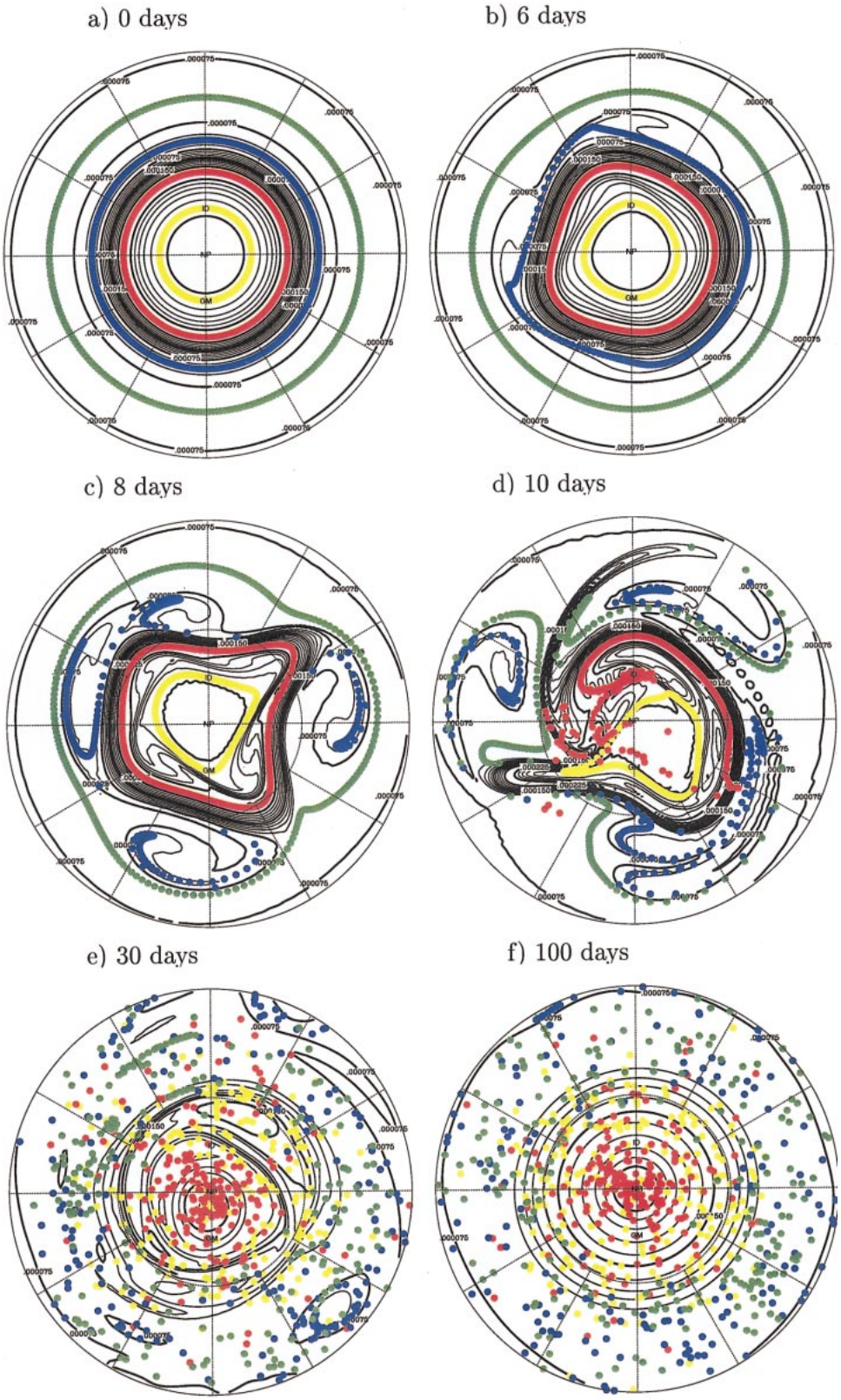

FIG. 2. Polar stereographic plots of the absolute vorticity field (in s^{-1}) and tracer positions for selected snapshots of experiment 1A. The domain shown goes from 30°N to the North Pole.

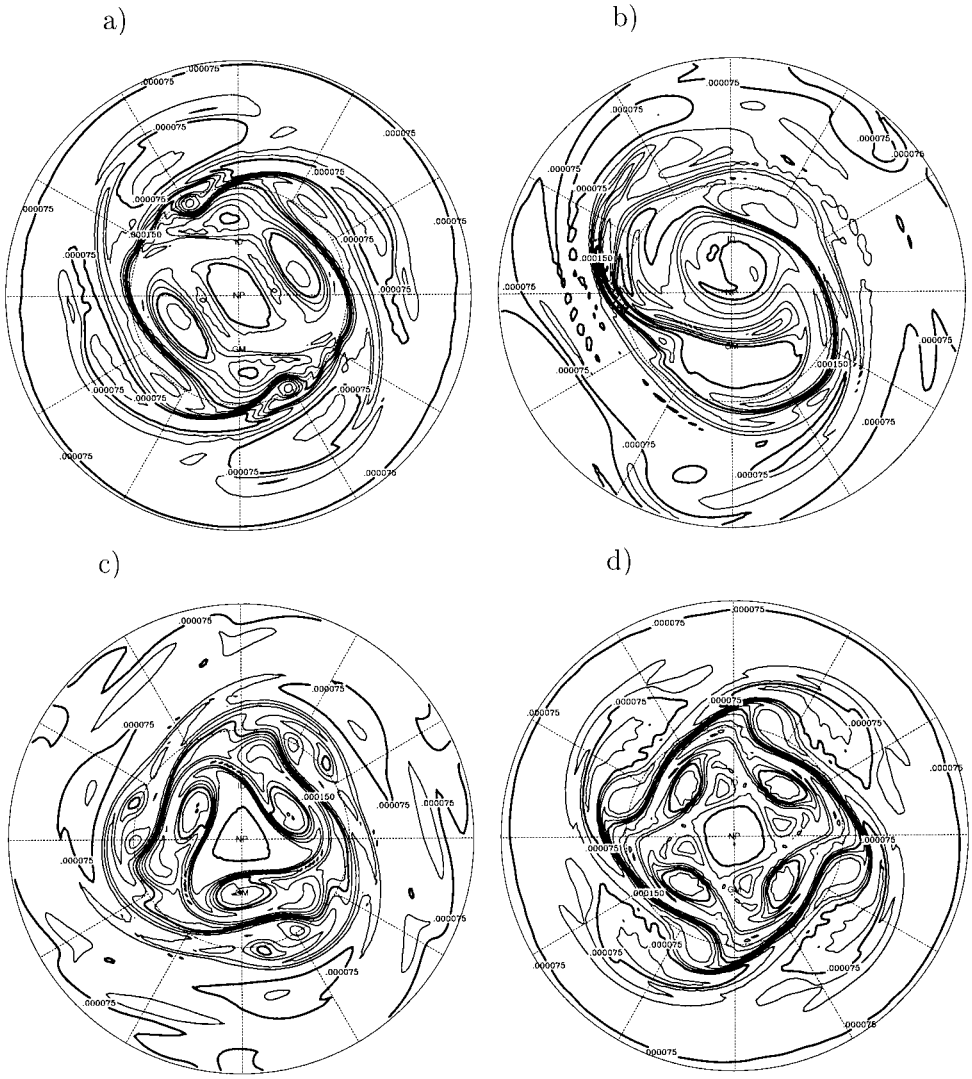

FIG. 3. Polar stereographic plots of the absolute vorticity field (in s^{-1}) at $t = 10$ days for the sech-type jet experiments with the different initial perturbations of Table 1. The display of tracers is omitted. The domain shown goes from 30°N to the North Pole. (a) Experiment 1B, (b) experiment 1C, (c) experiment 1D, (d) experiment 1E.

number of parcels (250) of each color and taking into account the area coverage relative to the initial position. In this way they can be directly compared with the predictions for the respective density functions $\rho_l(\phi)$ given by maximum entropy theory. Recall that the density function $\rho_l(\phi)$ gives the probability of finding the absolute vorticity value $\hat{\zeta}_l$ within a small neighborhood as a function of latitude. Figure 4 shows that green air parcels are preferentially redistributed northward of blue air parcels, while red air parcels mostly end up poleward of yellow air parcels, contrary to their initial positions. The density functions of maximum entropy theory show a remarkable agreement with the green, yellow, and red air parcels positions, but the blue air parcels have a wider distribution than that predicted by maximum entropy theory.

At $t = 100$ days the kinetic energy for experiment 1A has decreased 1.5% from its initial value (Fig. 5), with most of the decrease occurring after $t = 10.0$ days. The absolute enstrophy curve for experiment 1A has a steep decay between 10 and 25 days, which coincides with the wave breaking and filamentation of vorticity countours. After $t = 25$ days the absolute enstrophy slightly decreases, finishing at $t = 100$ days at 96.4% of its initial value.

Figure 6 compares the zonal wind profile for the average of the five direct numerical integrations at 100 days with the three theoretical predictions. All three predictions show good agreement for the value of the wind maximum ($\sim$65 m s^{-1}), which has decreased from its initial value of 91 m s^{-1}. The minimum enstrophy predictions reproduce very well the zonal wind distri-

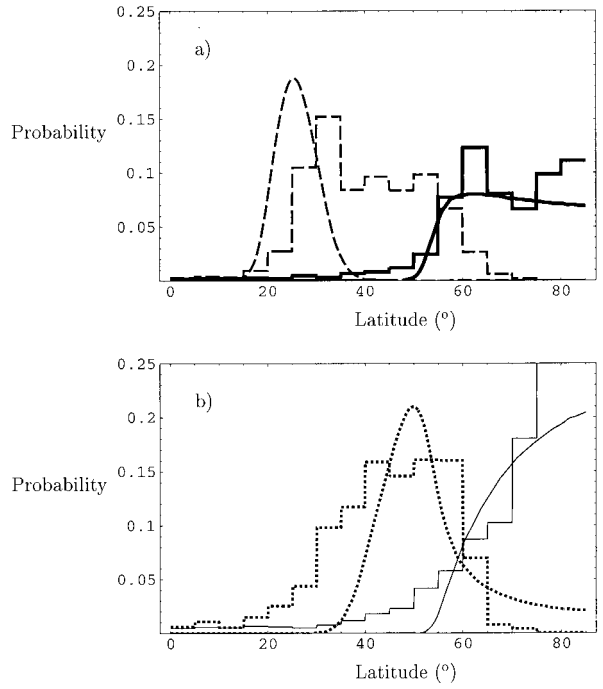

FIG. 4. Ensemble of tracer positions as a function of latitude for $t = 100$ days of the direct numerical integrations for experiments 1A–E. The histograms refer to the positions counted at 5° latitude intervals and taking into account area coverage relative to initial position, displayed together with their respective density function (smooth curves). The line code is as follows: Blue tracers, dashed line; yellow tracers, thick solid line; green tracers, dotted line; red tracers, thin solid line.

bution with an overlaping of the curves at high northern latitudes, while the maximum entropy prediction is shifted southward by about 10°.

The predictions of the absolute vorticity profile are shown in Fig. 7. The best agreement is for the minimum enstrophy curves; minEF-$\mathcal{E}$ predicts a southern mixing edge of 31.9°N and closely follows the direct numerical integration results. The absolute vorticity given by maximum entropy theory has a lower maximum than in the initial condition, which can be interpreted as the macroscopic view of strong mixing of vorticity levels for high northern latitudes. The minEF-$\mathcal{M}$ absolute vorticity curve shows good agreement with the time integration between 55°N and the North Pole. The actual absolute enstrophy value at $t = 100$ days for the average of the five direct numerical integrations is 96.55% of the initial value, while it is 96.37% for minEF-$\mathcal{E}$ and 96.43% for minEF-$\mathcal{M}$.

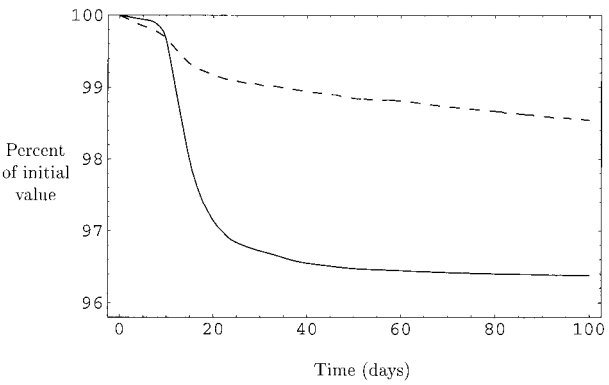

FIG. 5. Time dependence of the kinetic energy (dashed line) and absolute enstrophy (continuous line) relative to their initial values for experiment 1A.

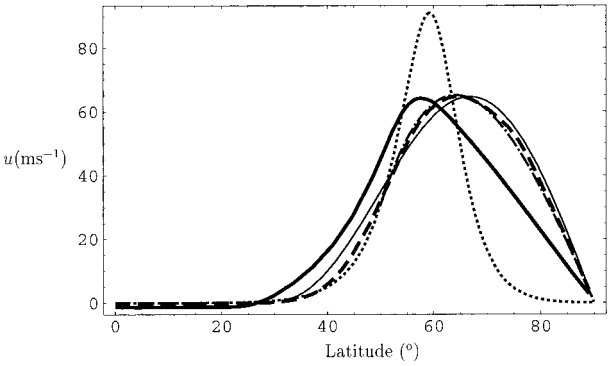

FIG. 6. Zonal wind profiles for experiment 1. Initial condition: dotted line. Averaged (experiments 1A–E) direct numerical integrations at $t = 100$ days: dashed line. MinEF-$\mathcal{E}$: thin solid line. Maximum entropy prediction: thick solid line. MinEF-$\mathcal{M}$: dash–dotted line.

b. *Experiment 2: Tanh-type jet*

Now consider the tanh-type jet given by (5.2), with the parameters $U = 180$ m s^{-1}, $\phi_0 = 45$°N, and $B = 6$°. This corresponds to the experiment reported by Ishioka and Yoden (1994) in their Fig. 6b. The associated absolute vorticity is given by

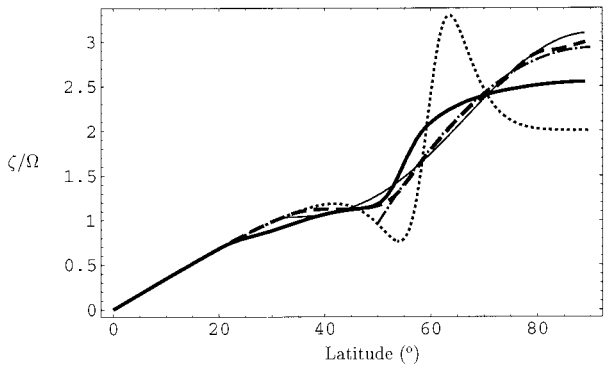

FIG. 7. Absolute vorticity profiles for experiment 1. Initial condition: dotted line. Averaged (experiments 1A–E) direct numerical integrations at $t = 100$ days: dashed line. MinEF-$\mathcal{E}$ [from Eq. (3.16)]: thin solid line. Maximum entropy prediction [from Eq. (4.1)]: thick solid line. MinEF-$\mathcal{M}$ [from Eq. (3.8)]: dash–dotted line.

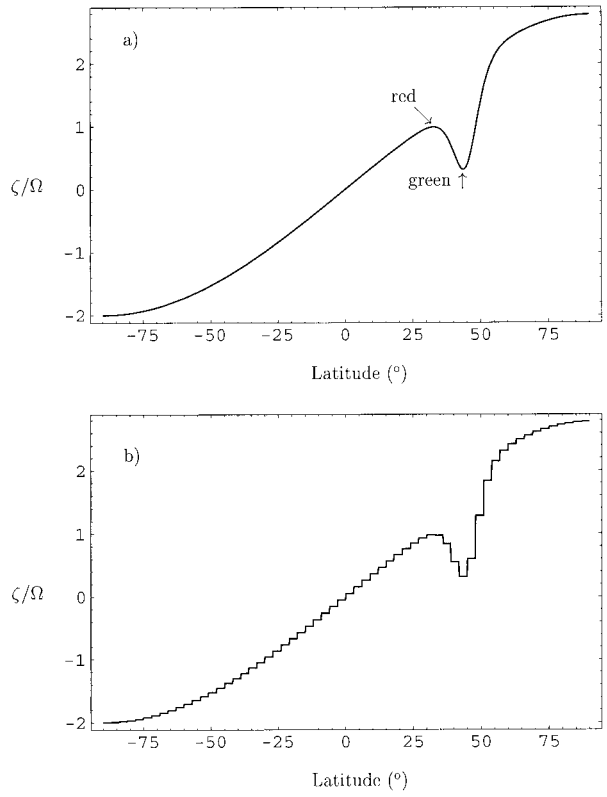

FIG. 8. Initial absolute vorticity profiles for experiment 2: (a) Direct numerical integration and (b) Maximum entropy theory. The arrows denote the initial positions of the colored tracers shown in Fig. 9.

$$\zeta_0(\phi) = \frac{U}{a}\left[\left(1 + \tanh\frac{\phi - \phi_0}{B}\right)\sin\phi - \frac{\left(\operatorname{sech}\frac{\phi - \phi_0}{B}\right)^2 \cos\phi}{2B}\right] + 2\Omega \sin\phi. \quad (5.6)$$

A plot of the initial absolute vorticity $\zeta_0(\phi)$ is shown in Fig. 8a. The discretized version, with the 60 vorticity levels used as initial condition for the maximum entropy prediction, is shown in Fig. 8b. The absolute vorticity profile $\zeta_0(\phi)$ has a relative maximum at 32.8°N and a relative minimum at 43.7°N. Ishioka and Yoden (1994) reported wavenumber 4 as the most unstable with an *e*-folding time of 0.78 day and a period of 2.03 days. Wavenumbers 1 and 7 are stable. Wavenumbers 3 and 4 have comparable values of the *e*-folding time.

Figure 9 is a Northern Hemisphere polar stereographic projection of the absolute vorticity field evolution of experiment 2A. This run includes the computation of 1000 air parcel trajectories initially uniformily distributed in two zonal rings, with 500 red parcels located at the relative maximum of the initial vorticity field (ϕ = 32.8°N), and 500 green parcels located at the relative minimum of ζ_0 at ϕ = 43.7°N. At t = 4.5 days the deformation of the initially circular contours is evident, creating two vorticity contour folds of the ''cat's eye'' type (Killworth and McIntyre 1985). At t = 6 days further folding has created pools of relatively low vorticity; these pools contain a large number of green parcels. Filamentation of the vortex edge (defined here as the region with the maximum absolute vorticity gradient) is also occurring. A strong deformation of the region of red particles is evident, with a tendency for these parcels to approach the vortex edge.

At t = 8.0 days three pools of green parcels have emerged and a triangular shape of the polar vortex edge has arisen with long vorticity filaments emanating from the vertices. At this time most of the red parcels have been advected poleward and are close to the vortex edge. At later times (t = 10 to 30 days) the polar vortex edge has an elliptical shape indicating a strong restoring mechanism towards axisymmetry after the deformations suffered earlier. On the other hand, the vortices which contain green parcels become elongated and begin to diffuse out and mix at low latitudes. As in experiment 1A, most of the mixing takes place in a period of about 25 days. This simulation stops at t = 100 days when zonal symmetry has returned, especially at high latitudes. The polar vortex is almost centered at the North Pole and is surrounded by a region where red parcels outnumber green parcels, while a ring of green parcels is evident in the region between 10° and 20°N. Note that inside the polar vortex edge there are few colored parcels, showing that the core of the polar vortex has behaved as a region isolated from midlatitude air intrusions.

The probability of finding a colored parcel within the neighborhood of a particular latitude for the ensemble of perturbations of the tanh-type jet (experiments 2A–E) is shown in Fig. 10, together with the respective density functions given by the maximum entropy prediction. The maximum probability for green tracers is located between 10° and 20°N, south of their initial position at 43.7°N. The maximum probability for red parcels is between 45° and 50°N, north of their initial position at 32.8°N. Notice the zero frequency of colored air parcel positions north of 60°N, which implies that ''surf zone'' air is not mixed across the high vorticity gradient zone. There is a good fit between the red parcel positions and the corresponding density function in the magnitude, width, and location of the tracers, as well as in its zero value north of 60°N. The comparison between green tracer positions and its density function shows good agreement in the position and magnitude of maximum frequency, but not in the width of the curves.

Figure 11 is the time series of the total kinetic energy (dashed line) and total absolute enstrophy (continuous line) relative to their initial values for the direct numerical integration of experiment 2A. The kinetic en-

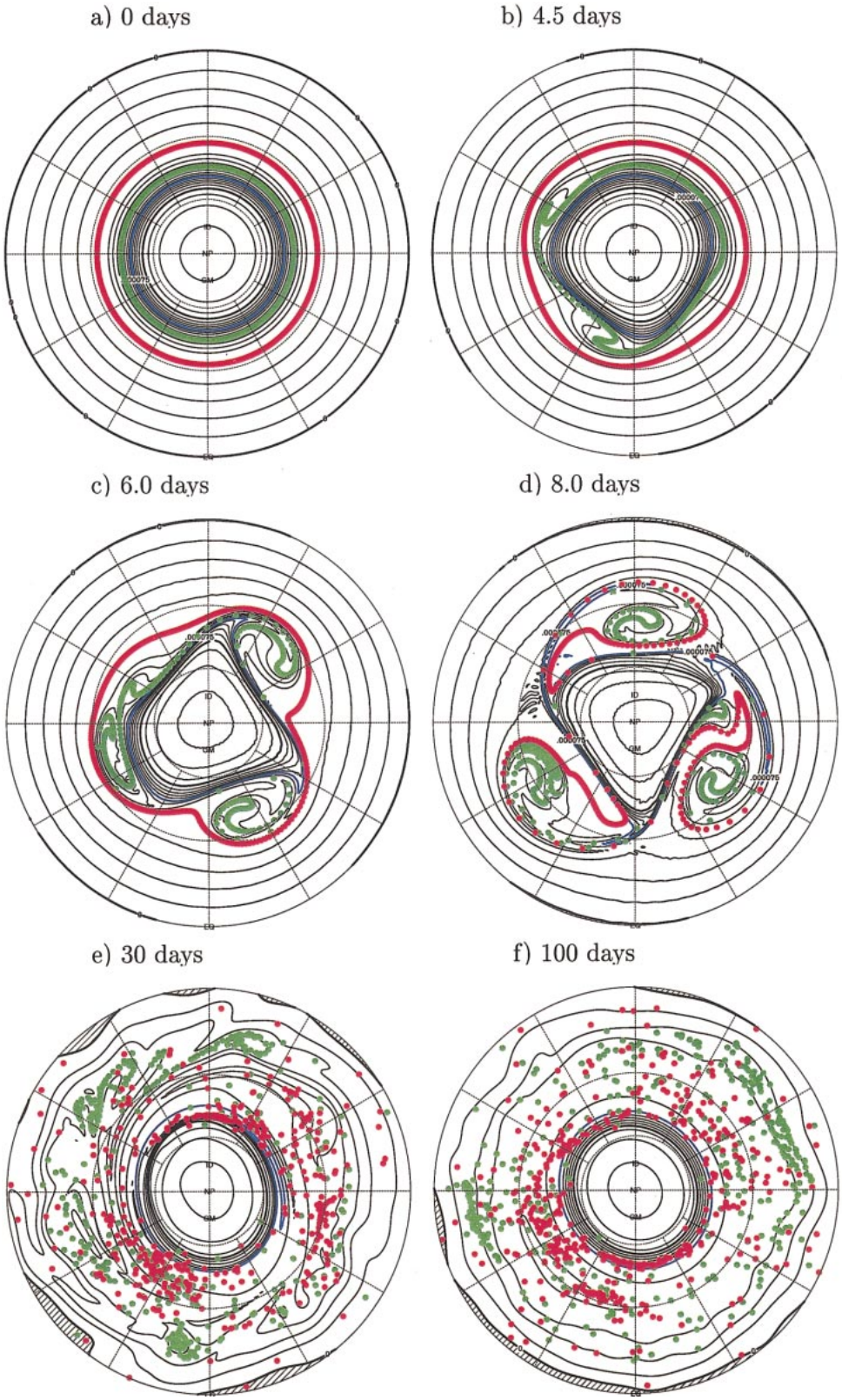

FIG. 9. Northern Hemisphere polar stereographic plots of the absolute vorticity field (in s^{-1}) and tracer positions for selected snapshots of experiment 2A.

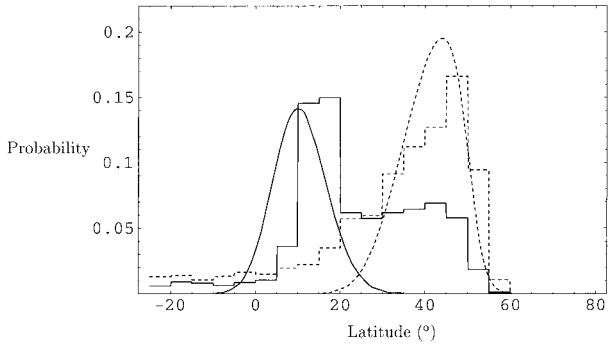

FIG. 10. Ensemble of tracer positions as a function of latitude for $t = 100$ days of the direct numerical integrations for experiments 2A–E. The histograms refer to the positions counted at 5° latitude intervals and taking into account area coverage relative to initial position, displayed together with their respective density function (smooth curves). The line code is as follows: Green tracers, solid line; red tracers, dashed line.

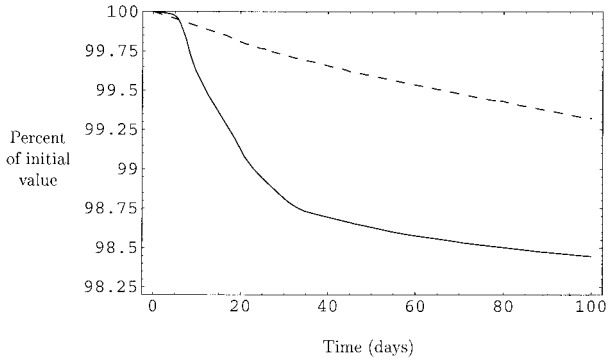

FIG. 11. Time dependence of the kinetic energy (dashed line) and absolute enstrophy (continuous line) relative to their initial values for experiment 2A.

ergy curve shows a steady dissipation, reducing its initial value by approximately 0.75% at the end of the integration. The absolute enstrophy curve shows a sharp reduction of around 1.25% between day 5 and day 30, which is the period of maximum nonlinear behavior of the flow. From days 30 to 100, the absolute enstrophy curve shows a further reduction of approximately 0.25% but with signs of approaching an asymptotic value, which is consistent with the main hypothesis of minimum enstrophy theory described in section 3.

A comparison of the zonal wind profiles for this experiment (Fig. 12) shows that, in the averaged set of direct numerical integrations, the initial zonal wind is only modified south of 55°N. the velocity maximum is reduced by approximately 5 m s^{-1} while the jet broadens towards the south, creating a weak easterly flow between 10°–25°N and between the South Pole and 50°S. The maximum entropy prediction has an easterly flow from the South Pole to 15°N, with a broadening of the jet and a slight modification of the initial condition at high northern latitudes, with a decrease of the initial wind maximum of the order of 10 m s^{-1}. The minimum enstrophy prediction with constant energy and two edges broadens the velocity profile, predicting mixing from 17.7° to 64.8°N, reducing the wind maximum more than the maximum entropy prediction. For the minimum enstrophy prediction with constant angular momentum and two edges no solution was found.

A comparison of the absolute vorticity profiles is made in Fig. 13a. The predictions remove the reversal of the absolute vorticity gradient. The minimum enstrophy predictions with one edge (not shown) violate the conservation of vorticity, predicting a maximum of ζ higher than the maximum in the initial condition. This is a failure in the assumption that vorticity will be mixed all the way to the North Pole. The minimum enstrophy prediction with constant energy and two edges has a better fit in comparison with the direct numerical integration. The best prediction for this experiment is that given by the maximum entropy theory, which shows relatively good agreement with the direct numerical integration in both the Northern and Southern Hemispheres. Note that, while the maximum entropy results are global, the minimum enstrophy results are restricted to a portion of the sphere. The predicted absolute enstrophy for the minEF-$\mathcal{E}$ with two edges is 98.34% of initial value, compared with the value of 98.49% at $t = 100$ days for the ensemble of numerical integrations. Figure 13b shows the same comparisons, but for the relative vorticity profiles. Both maximum entropy and minEF-$\mathcal{E}$ capture well the change of the flow at midlatitudes in the Northern Hemisphere, and maximum entropy predicts well the relative vorticity change in the Southern Hemisphere, but has a less accurate prediction north of 60°N.

6. Summary and discussion

Barotropic instability of the polar night jet has been investigated using nonlinear time integrations of a nondivergent barotropic model on the sphere. The mecha-

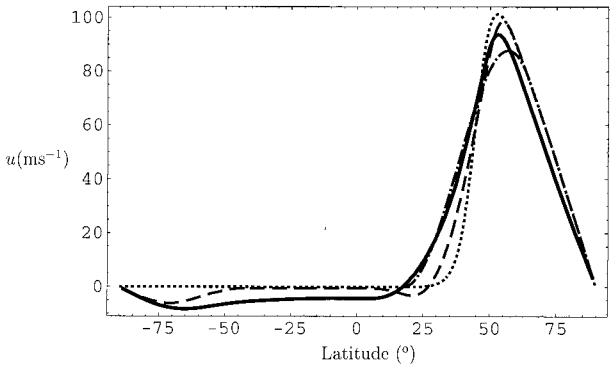

FIG. 12. Zonal wind profiles for experiment 2. Initial condition: dotted line. Averaged (experiments 2A–E) direct numerical integrations at $t = 100$ days: dashed line. MinEF-$\mathcal{E}$ with two edges: dash–dotted line. Maximum entropy prediction: thick solid line.

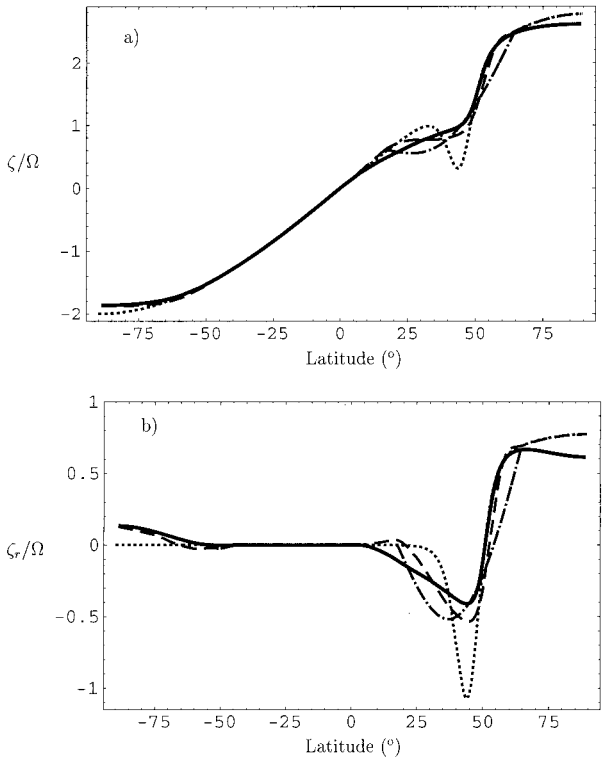

FIG. 13. (a) Absolute vorticity profiles for experiment 2. Initial condition: dotted line. Averaged (experiments 2A–E) direct numerical integrations at $t = 100$ days: dashed line. MinEF-$\mathcal{E}$ with two edges [from Eq. (B.7)]: dash–dotted line. Maximum entropy prediction [from Eq. (4.1)]: thick solid line. (b) Same as (a) but for relative vorticity.

nism by which the flow instabilities are removed is ''wave breaking'' and mixing of vorticity in regions where the absolute vorticity gradient has a sign reversal. Most of the nonlinear phase lasts approximately 25 days and is marked by wave breaking, filamentation of vorticity contours, dispersion of air parcel tracers, and a rapid decrease of the total enstrophy of the flow. This nonlinear activity is followed by a quasi-steady state of the fluid, which in our experiments is characterized by an almost zonally symmetric flow that has a small and steady decay of kinetic energy and an approach to an asymptotic value of enstrophy. Theoretical predictions of this end state, given by the maximum entropy and minimum enstrophy theories, have been compared with the zonal average of absolute vorticity and zonal wind at $t = 100$ days of two ensembles of direct numerical integrations. The precise evolution of the flow was sensitive to the initial perturbation in both sets of ensemble experiments. This sensitivity was apparent in the detailed distribution of the vorticity field and tracers even at very long times ($\sim$100 days). Thus, statistical predictions can be a natural tool in the study of this type of problem.

The minimum enstrophy predictions showed very good agreement in experiment 1, where nonlinear behaviour is restricted to a polar cap. Predictions from maximum entropy theory demonstrated good skill in experiment 2, which has substantial changes everywhere except the north polar cap. The above predictions have been compared with the zonal average of an ensemble of five direct numerical integrations. Therefore, any deviation from zonal symmetry of the flow has an impact on the comparisons. The predictions are based upon the initial condition, and since we are using a numerical model with a hyperdiffusive term, the energy of the flow will be reduced over time, thus changing the actual energy value of the equilibrium state. Flows with equilibrium states relatively far from the initial condition involve a significant decrease of energy before a steady state is reached. In those cases predictions that maintain a constant energy (like minEF-$\mathcal{E}$ and maximum entropy) will have reduced skill when compared with the nonlinear time integration.

Compared to the minEF theories, maximum entropy theory gives us an additional source of information with the density functions $\rho_l(\phi)$, which in a probabilistic sense tell us how the vorticity field (and therefore the mass field) has been redistributed at the equilibrium state. The density functions showed good skill predicting several of the colored air parcel spatial distributions in the above experiments. Also, from a local point of view, density functions give us a way to determine the degree of mixing of initially well separated air masses, information that could be valuable in tracing atmospheric chemical components.

The results presented above show that maximum entropy theory provided more accurate predictions than minimum enstrophy theory for the flow that changed over the whole domain, while minimum enstrophy theory did better for flow that changed just over a localized region of the sphere. From the computational point of view, minimum enstrophy solutions were obtained faster (in few minutes) compared to the maximum entropy iterative code, which generally takes a couple of hours to converge on a Pentium I processor. Chavanis and Sommeria (1996) made a theoretical comparison of minimum enstrophy and maximum entropy theories, and showed that in the limit of strong mixing and within a given subdomain of an infinite plane, a maximum entropy state and a minimum enstrophy state are equivalent. Thus, we could expect that both theories will have similar predictions in problems with strong mixing and where their computational methods have the same assumptions.

The ideas of maximum entropy theory have been further developed by Chavanis and Sommeria (1997), Robert and Rosier (1997), and Kazantsev et al. (1998), who used the maximum entropy production principle (MEPP). This principle states that during the relaxation toward equilibrium, the system tends to maximize its rate of entropy production while it satisfies all the integral constraints imposed by the dynamics. The argument leads to a set of relaxation equations describing

flow evolution toward the maximum entropy equilibrium state. The main difference from the Navier–Stokes equations is that the MEPP conserves the energy and all the constants of the motion of the Euler equations. This new theory can be applied to forced problems and leads to a natural modeling of the small scales in turbulent flows, which may be relevant for meteorological and oceanographic applications.

In closing we note that it is possible to generalize the maximum entropy arguments from the nondivergent barotropic model on the sphere to the quasi-static primitive equation model of inviscid adiabatic flow on the sphere. A key ingredient in the argument is the use of the isentropic coordinate in the vertical. This generalization yields maximum entropy predictions of end states resulting from baroclinically unstable initial states.

Acknowledgments. We would like to express our thanks to Michael Montgomery, William Gray, Gerald Taylor, and James Kossin for their useful comments and suggestions. This work was supported by a National Autonomous University of México (UNAM) scholarship through the Dirección General de Asuntos del Personal Académico, by the National Science Foundation under Grants ATM-9729970 and ATM-0087072, and by NOAA under Grant NA67RJ0152.

APPENDIX A

Minimum Enstrophy Flow with Fixed Angular Momentum and Two Edges (MinEF-$\mathcal{M}$)

Let us assume that vorticity mixing is confined to a zonal strip with unknown south edge μ_s and unknown north edge μ_n. In the regions $-1 \le \mu \le \mu_s$ and $\mu_n \le \mu \le 1$, the final zonally symmetric flow $U(\mu)$ is equal to the initial zonally symmetric flow $U_0(\mu)$ and the final vorticity $\zeta(\mu)$ is equal to the initial vorticity $\zeta_0(\mu)$. Requiring $U(\mu)$ to be a continuous function, we have

$$U(\mu_s) = U_0(\mu_s), \qquad U(\mu_n) = U_0(\mu_n) \tag{A.1}$$

as boundary conditions on the final flow in the mixed region.

We now explore the hypothesis that the final flow can be found by maximizing the enstrophy deficit (relative to the initial enstrophy) subject to the constraint of angular momentum invariance; that is,

$$\text{maximize} \quad \int_{\mu_s}^{\mu_n} \frac{1}{2}(\zeta_0^2 - \zeta^2)\, d\mu, \tag{A.2}$$

subject to

$$\int_{\mu_s}^{\mu_n} (U_0 - U)\, d\mu = 0. \tag{A.3}$$

To solve this problem we now vary the mixing edges μ_s and μ_n, the zonal wind profile $U(\mu)$, and the associated vorticity profile $\zeta(\mu)$ in search of that zonal flow that has maximum enstrophy deficit (i.e., minimum enstrophy) for fixed angular momentum. Since μ_s and μ_n are unknown, their first variations are related to the first variations in U at those latitudes by $\delta U(\mu_s) = [U_0'(\mu_s) - U'(\mu_s)]\delta\mu_s = -a[\zeta_0(\mu_s) - \zeta(\mu_s)]\delta\mu_s$ and $\delta U(\mu_n) = [U'_0(\mu_n) - U'(\mu_n)]\delta\mu_n = -a[\zeta_0(\mu_n) - \zeta(\mu_n)]\delta\mu_n$. Using these results, introducing the Lagrange multiplier $-\gamma$, and recalling Leibniz's rule, the variational problem is

$$\begin{aligned} 0 &= \delta \int_{\mu_s}^{\mu_n} \left[\frac{1}{2}(\zeta_0^2 - \zeta^2) - \gamma(U_0 - U)\right] d\mu \\ &= \int_{\mu_s}^{\mu_n} \left(-\frac{d\zeta}{ad\mu} + \gamma\right)\delta U\, d\mu + \frac{1}{2}[\zeta_0(\mu_n) - \zeta(\mu_n)]^2\delta\mu_n \\ &\quad - \frac{1}{2}[\zeta_0(\mu_s) - \zeta(\mu_s)]^2\delta\mu_s. \end{aligned} \tag{A.4}$$

For the independent variations $\delta\mu_s$ and $\delta\mu_n$, we obtain the transversality conditions

$$\zeta(\mu_s) = \zeta_0(\mu_s), \qquad \zeta(\mu_n) = \zeta_0(\mu_n). \tag{A.5}$$

For the independent variation δU, we obtain the Euler–Lagrange equation

$$\frac{d\zeta}{ad\mu} = \gamma \quad \text{for } \mu_s \le \mu \le \mu_n. \tag{A.6}$$

Integrating (A.6) and enforcing the transversality conditions (A.5), we find that the final vorticity satisfies

$$\zeta(\mu) = \zeta_0(\mu_n)\left(\frac{\mu - \mu_s}{\mu_n - \mu_s}\right) + \zeta_0(\mu_s)\left(\frac{\mu_n - \mu}{\mu_n - \mu_s}\right) \quad \text{for } \mu_s \le \mu \le \mu_n, \tag{A.7}$$

if the Lagrange multiplier γ takes on the value

$$\gamma = \frac{\zeta_0(\mu_n) - \zeta_0(\mu_s)}{a(\mu_n - \mu_s)}, \tag{A.8}$$

which is the constant vorticity gradient across the mixed region.

Since $d[U + \Omega a(1 - \mu^2)]/d\mu = -a\zeta$, the solution for $U(\mu)$ can be written as

$$\begin{aligned} &U(\mu) + \Omega a(1 - \mu^2) \\ &= [U_0(\mu_s) + \Omega a(1 - \mu_s^2)]\left(\frac{\mu_n - \mu}{\mu_n - \mu_s}\right) \\ &\quad + [U_0(\mu_n) + \Omega a(1 - \mu_n^2)]\left(\frac{\mu - \mu_s}{\mu_n - \mu_s}\right) \\ &\quad - \frac{1}{2}a\left[\frac{\zeta_0(\mu_n) - \zeta_0(\mu_s)}{\mu_n - \mu_s}\right][\mu^2 - (\mu_s + \mu_n)\mu + \mu_s\mu_n] \end{aligned} \tag{A.9}$$

for $\mu_s \le \mu \le \mu_n$. Note that (A.9) satisfies the boundary conditions (A.1). The linear vorticity function obtained by taking $d/d\mu$ of (A.9) has the same constant $d\zeta/d\mu$ value as given by (A.6) and (A.8). Requiring that (A.7) and (A.9) lead to consistent values of $\zeta(\mu)$ at one point in the mixing region (e.g., the point $\mu = 1/2\ (\mu_s + \mu_n)$) leads to the relation

$$\frac{1}{2}[\zeta_0(\mu_s) + \zeta_0(\mu_n)] = \frac{[U_0(\mu_s) + \Omega a(1-\mu_s^2)] - [U_0(\mu_n) + \Omega a(1-\mu_n^2)]}{a(\mu_n - \mu_s)}. \tag{A.10}$$

For given initial conditions $U_0(\mu)$ and $\zeta_0(\mu)$, (A.10) constitutes one of the two transcendental relations required for the determination of the mixing edges μ_s and μ_n. The other relation is obtained by substituting (A.9) into the angular momentum constraint (A.3). We can now summarize the argument as follows. Given an initial unstable zonally symmetric flow with zonal wind $U_0(\mu)$ and vorticity $\zeta_0(\mu)$, first determine μ_s and μ_n from (A.3) and (A.10). The final adjusted vorticity profile $\zeta(\mu)$ and zonal wind profile $U(\mu)$ are then given by (A.7) and (A.9).

APPENDIX B

Minimum Enstrophy Flow with Fixed Energy and Two Edges (MinEF-$\mathcal{E}$)

We assume that, in the regions $-1 \le \mu \le \mu_s$ and $\mu_n \le \mu \le 1$, the final angular velocity $\omega(\mu)$ is equal to the initial angular velocity $\omega_0(\mu)$, so that in particular

$$\omega(\mu_s) = \omega_0(\mu_s), \qquad \omega(\mu_n) = \omega_0(\mu_n). \tag{B.1}$$

We now explore the hypothesis that the final flow can be found by maximizing the enstrophy deficit subject to the constraint of kinetic energy invariance; that is,

$$\text{maximize} \quad \int_{\mu_s}^{\mu_n} \frac{1}{2}(\zeta_0^2 - \zeta^2)\, d\mu, \tag{B.2}$$

subject to

$$\int_{\mu_s}^{\mu_n} \frac{1}{2}(u_0^2 - u^2)\, d\mu = 0. \tag{B.3}$$

We now vary μ_s, μ_n, the zonal wind profile $u(\mu)$ and the associated vorticity profile $\zeta(\mu)$ in search of that zonal flow which has maximum enstrophy deficit for fixed energy. Introducing the Lagrange multiplier β, the variational problem is

$$\begin{aligned} 0 &= \delta \int_{\mu_s}^{\mu_n} \frac{1}{2}[\zeta_0^2 - \zeta^2 + \beta(u_0^2 - u^2)]\, d\mu \\ &= -\int_{\mu_s}^{\mu_n} (\zeta - \beta\psi)\delta\zeta\, d\mu \\ &\quad + \frac{1}{2}[\zeta_0(\mu_n) + \zeta(\mu_n) - 2\beta\psi(\mu_n)] \\ &\quad \times [\zeta_0(\mu_n) - \zeta(\mu_n)]\delta\mu_n \\ &\quad - \frac{1}{2}[\zeta_0(\mu_s) + \zeta(\mu_s) - 2\beta\psi(\mu_s)] \\ &\quad \times [\zeta_0(\mu_s) - \zeta(\mu_s)]\delta\mu_s. \end{aligned} \tag{B.4}$$

For the independent variations $\delta\mu_s$ and $\delta\mu_n$, we again obtain the transversality conditions

$$\zeta(\mu_s) = \zeta_0(\mu_s), \qquad \zeta(\mu_n) = \zeta_0(\mu_n). \tag{B.5}$$

For the independent variation $\delta\zeta$, we obtain $\zeta = -a^{-2}\alpha(\alpha+1)\psi$ for $\mu_s \le \mu \le \mu_n$, where α is defined in terms of the Lagrange multiplier by $\alpha(\alpha+1) = -\beta a^2$. When written in terms of the streamfunction, this linear relation between ζ and ψ takes the form

$$\begin{aligned} (1-\mu^2)\frac{d^2\psi}{d\mu^2} - 2\mu\frac{d\psi}{d\mu} + \alpha(\alpha+1)\psi \\ = -2\Omega a^2\mu \quad \text{for } \mu_s \le \mu \le \mu_n. \end{aligned} \tag{B.6}$$

The general solution of (B.6) is $\psi(\mu) = AP_\alpha(\mu) + BQ_\alpha(\mu) + 2\Omega a^2\mu/[2 - \alpha(\alpha+1)]$, where $P_\alpha(\mu)$ and $Q_\alpha(\mu)$ are the Legendre functions of (noninteger) order α, and A and B are constants. The Legendre function $P_\alpha(\mu)$ is not finite at $\mu = -1$ while the Legendre function $Q_\alpha(\mu)$ is not finite at $\mu = 1$. If $-1 < \mu_s$ and $\mu_n < 1$, both Legendre functions are needed in the construction of the general solution to (B.6). Since $\zeta(\mu) = -a^{-2}\alpha(\alpha+1)\psi$, the general solution for the vorticity is $\zeta(\mu) = -a^{-2}\alpha(\alpha+1)\{AP_\alpha(\mu) + BQ_\alpha(\mu) + 2\Omega a^2\mu/[2 - \alpha(\alpha+1)]\}$. The constants A and B can now be obtained by enforcing the transversality conditions (B.5). This results in

$$\begin{aligned} \zeta(\mu) &= \left[\zeta_0(\mu_n) - \left(\frac{\alpha(\alpha+1)2\Omega\mu_n}{\alpha(\alpha+1) - 2}\right)\right] \\ &\quad \times \left[\frac{Q_\alpha(\mu_s)P_\alpha(\mu) - P_\alpha(\mu_s)Q_\alpha(\mu)}{Q_\alpha(\mu_s)P_\alpha(\mu_n) - P_\alpha(\mu_s)Q_\alpha(\mu_n)}\right] \\ &\quad + \left[\zeta_0(\mu_s) - \left(\frac{\alpha(\alpha+1)2\Omega\mu_s}{\alpha(\alpha+1) - 2}\right)\right] \\ &\quad \times \left[\frac{P_\alpha(\mu_n)Q_\alpha(\mu) - Q_\alpha(\mu_n)P_\alpha(\mu)}{P_\alpha(\mu_n)Q_\alpha(\mu_s) - Q_\alpha(\mu_n)P_\alpha(\mu_s)}\right] \\ &\quad + \frac{\alpha(\alpha+1)2\Omega\mu}{\alpha(\alpha+1) - 2}, \end{aligned} \tag{B.7}$$

for $\mu_s \le \mu \le \mu_n$. Since the angular velocity is related to the streamfunction by $\omega(\mu) = -a^{-2}(d\psi/d\mu)$, we can also determine the constants A and B by enforcing (B.1). This results in

$$\omega(\mu) = \left[\omega_0(\mu_n) - \frac{2\Omega}{\alpha(\alpha+1)-2}\right] \times \left[\frac{Q'_\alpha(\mu_s)P'_\alpha(\mu) - P'_\alpha(\mu_s)Q'_\alpha(\mu)}{Q'_\alpha(\mu_s)P'_\alpha(\mu_n) - P'_\alpha(\mu_s)Q'_\alpha(\mu_n)}\right] + \left[\omega_0(\mu_s) - \frac{2\Omega}{\alpha(\alpha+1)-2}\right] \times \left[\frac{P'_\alpha(\mu_n)Q'_\alpha(\mu) - Q'_\alpha(\mu_n)P'_\alpha(\mu)}{P'_\alpha(\mu_n)Q'_\alpha(\mu_s) - Q'_\alpha(\mu_n)P'_\alpha(\mu_s)}\right] + \frac{2\Omega}{\alpha(\alpha+1)-2}. \quad \text{(B.8)}$$

Because $\zeta(\mu)$ and $\omega(\mu)$ are related by $\zeta = 2\Omega\mu - d[(1-\mu^2)\omega]/d\mu$, consistency between (B.7) and (B.8) requires

$$\alpha(\alpha+1)\left[\frac{P_\alpha(\mu_n)Q_\alpha(\mu_s) - P_\alpha(\mu_s)Q_\alpha(\mu_n)}{P'_\alpha(\mu_n)Q'_\alpha(\mu_s) - P'_\alpha(\mu_s)Q'_\alpha(\mu_n)}\right] = \left[\frac{C(\mu_n)Q_\alpha(\mu_s) - C(\mu_s)Q_\alpha(\mu_n)}{D(\mu_n)Q'_\alpha(\mu_s) - D(\mu_s)Q'_\alpha(\mu_n)}\right], \quad \text{(B.9)}$$

$$\alpha(\alpha+1)\left[\frac{P_\alpha(\mu_n)Q_\alpha(\mu_s) - P_\alpha(\mu_s)Q_\alpha(\mu_n)}{P'_\alpha(\mu_n)Q'_\alpha(\mu_s) - P'_\alpha(\mu_s)Q'_\alpha(\mu_n)}\right] = \left[\frac{C(\mu_n)P_\alpha(\mu_s) - C(\mu_s)P_\alpha(\mu_n)}{D(\mu_n)P'_\alpha(\mu_s) - D(\mu_s)P'_\alpha(\mu_n)}\right], \quad \text{(B.10)}$$

where $C(\mu) = \zeta_0(\mu) - [\alpha(\alpha+1)2\Omega\mu]/[\alpha(\alpha+1)-2]$ and $D(\mu) = \omega_0(\mu) - 2\Omega/[\alpha(\alpha+1)-2]$. For given initial conditions $\omega_0(\mu)$ and $\zeta_0(\mu)$, (B.9) and (B.10) constitute two of the three transcendental relations required for the determination of the mixing edges μ_s and μ_n and the Lagrange multiplier α. The other relation is obtained by substituting (B.8) into the energy constraint (B.3). We can summarize the MinEF-$\mathcal{E}$ argument as follows. Given an initial unstable zonal flow with angular velocity $\omega_0(\mu)$ and vorticity $\zeta_0(\mu)$, first determine α, μ_s, and μ_n from (B.3), (B.9), and (B.10). The final adjusted vorticity profile $\zeta(\mu)$ and angular velocity profile $\omega(\mu)$ are then given by (B.7) and (B.8).

REFERENCES

Bowman, K. P., and N. J. Mangus, 1993: Observations of deformation and mixing of the total ozone field in the antarctic polar vortex. *J. Atmos. Sci.,* **50,** 2915–2921.

Bretherton, F., and D. Haidvogel, 1976: Two-dimensional turbulence above topography. *J. Fluid Mech.,* **78,** 129–154.

Carnevale, G. F., J. C. McWilliams, Y. Pomeau, J. B. Weiss, and W. R. Young, 1991: Evolution of vortex statistics in two-dimensional turbulence. *Phys. Rev. Lett.,* **66,** 2735–2737.

——, ——, ——, ——, and ——, 1992: Rates, pathways, and end states of nonlinear evolution in decaying two-dimensional turbulence: Scaling theory versus selective decay. *Phys. Fluids A,* **4,** 1314–1316.

Chavanis, P. H., and J. Sommeria, 1996: Classification of self-organized vortices in two-dimensional turbulence: The case of a bounded domain. *J. Fluid Mech.,* **314,** 267–297.

——, and ——, 1997: Thermodynamical approach for small-scale parametrization in 2D turbulence. *Phys. Rev. Lett.,* **78,** 3302–3305.

——, and ——, 1998: Classification of robust isolated vortices in two-dimensional hydrodynamics. *J. Fluid. Mech.,* **356,** 259–296.

Cho, J. Y., and L. M. Polvani, 1996: The emergence of jets and vortices in freely evolving, shallow-water turbulence on a sphere. *Phys. Fluids,* **8,** 1531–1552.

Fjørtoft, R., 1953: On the changes in the spectral distribution of kinetic energy for two-dimensional non-divergent flow. *Tellus,* **5,** 225–230.

Fox, C., 1987: *An Introduction to the Calculus of Variations.* Dover Publications, 271 pp.

Hack, J. J., and R. Jakob, 1992: Description of a global shallow water model based on the transform method. NCAR Tech. Note NCAR/TN-343+STR, 39 pp.

Hartmann, D. L., 1983: Barotropic instability of the polar night jet stream. *J. Atmos. Sci.,* **40,** 817–835.

Ishioka, K., and S. Yoden, 1994: Non-linear evolution of a barotropically unstable circumpolar vortex. *J. Meteor. Soc. Japan,* **72,** 63–79.

Joyce, G., and D. Montgomery, 1973: Negative temperature states for the two-dimensional guiding-centre plasma. *J. Plasma Phys.,* **10,** 107–121.

Kazantsev, E., J. Sommeria, and J. Verron, 1998: Subgrid-scale eddy parameterization by statistical mechanics in a barotropic ocean model. *J. Phys. Oceanogr.,* **28,** 1017–1042.

Killworth, P. D., and M. E. McIntyre, 1985: Do Rossby-wave critical layers absorb, reflect or over-reflect? *J. Fluid Mech.,* **161,** 449–492.

Kuo, H. L., 1949: Dynamic instability of two-dimensional nondivergent flow in a barotropic atmosphere. *J. Meteor.,* **6,** 105–122.

Legras, B., and D. G. Dritschel, 1993: A comparison of the contour surgery and pseudospectral methods. *J. Comput. Phys.,* **104,** 287–302.

Leith, C. E., 1984: Minimum enstrophy vortices. *Phys. Fluids,* **27,** 1388–1395.

Matthaeus, W. H., and D. Montgomery, 1980: Selective decay hypothesis at high mechanical and magnetic Reynolds numbers. *Ann. N.Y. Acad. Sci.,* **357,** 203–222.

——, W. T. Stribling, D. Martinez, and S. Oughton, 1991: Selective decay and coherent vortices in two-dimensional incompressible turbulence. *Phys. Rev. Lett.,* **66,** 2731–2734.

McIntyre, M. E., 1982: How well do we understand the dynamics of stratospheric warmings? *J. Meteor. Soc. Japan,* **60,** 37–65.

——, and T. N. Palmer, 1983: Breaking planetary waves in the stratosphere. *Nature,* **305,** 593–600.

——, and ——, 1984: The 'surf zone' in the stratosphere. *J. Atmos. Terr. Phys.,* **46,** 825–849.

McWilliams, 1984: The emergence of isolated coherent vortices in turbulent flow. *J. Fluid Mech.,* **146,** 21–43.

Merilees, P. E., and H. Warn, 1975: On energy and enstrophy exchanges in two-dimensional non-divergent flow. *J. Fluid Mech.,* **69,** 625–630.

Miller, J., 1990: Statistical mechanics of Euler equations in two dimensions. *Phys. Rev. Lett.,* **65,** 2137–2140.

——, P. B. Weichman, and M. C. Cross, 1992: Statistical mechanics, Euler's equations, and Jupiter's red spot. *Phys. Rev. A,* **45,** 2328–2359.

Montgomery, D., W. H. Matthaeus, W. T. Stribling, D. Martinez, and

S. Oughton, 1992: Relaxation in two dimensions and the ''sinh-Poisson'' equation. *Phys. Fluids A,* **4,** 3–6.

Norton, W. A., 1994: Breaking Rossby waves in a model stratosphere diagnosed by a vortex-following coordinate system and a technique for advecting material contours. *J. Atmos. Sci.,* **51,** 654–673.

Onsager, L., 1949: Statistical hydrodynamics. *Nuovo Climento,* **6,** (Suppl.), 279–287.

Polvani, L. M., J. C. McWilliams, M. A. Spall, and R. Ford, 1994: The coherent structures of shallow-water turbulence: Deformation-radius effects, cyclone/anticyclone asymmetry and gravity-wave generation. *Chaos,* **4,** 177–186.

Robert, R., 1991: A maximum-entropy principle for two-dimensional perfect fluid dynamics. *J. Stat. Phys.,* **65,** 531–551.

——, and J. Sommeria, 1991: Statistical equilibrium states for two-dimensional flows. *J. Fluid Mech.,* **229,** 291–310.

——, and ——, 1992: Relaxation towards a statistical equilibrium state in two-dimensional perfect fluid dynamics. *Phys. Rev. Lett.,* **69,** 2776–2779.

——, and C. Rosier, 1997: The modeling of small scales in two-dimensional turbulent flows: A statistical mechanics approach. *J. Stat. Phys.,* **86,** 481–515.

Schubert, W. H., M. T. Montgomery, R. K. Taft, T. A. Guinn, S. R. Fulton, J. P. Kossin, and J. P. Edwards, 1999: Polygonal eyewalls, asymmetric eye contraction, and potential vorticity mixing in hurricanes. *J. Atmos. Sci.,* **56,** 1197–1223.

Sommeria, J., C. Staquet, and R. Robert, 1991: Final equilibrium state of a two-dimensional shear layer. *J. Fluid Mech.,* **233,** 661–689.

Turkington, B., and N. Whitaker, 1996: Statistical equilibrium computations of coherent structures in turbulent shear layers. *SIAM J. Sci. Comput.,* **17,** 1414–1433.

Van de Konijnenberg, J. A., J. B. Flór, and G. J. F. van Heijst, 1998: Decaying quasi-two-dimensional viscous flow on a square domain. *Phys. Fluids,* **10,** 595–606.

Waugh, D. W., and R. A. Plumb, 1994: Contour advection with surgery: A technique for investigating finescale structure in tracer transport. *J. Atmos. Sci.,* **51,** 530–540.

Whitaker, N., and B. Turkington, 1994: Maximum entropy states for rotating vortex patches. *Phys. Fluids,* **6,** 3963–3973.

Yoden, S., and M. Yamada, 1993: A numerical experiment on two-dimensional decaying turbulence on a rotating sphere. *J. Atmos. Sci.,* **50,** 631–643.

Young, W. R., 1987: Selective decay of enstrophy and the excitation of barotropic waves in a channel. *J. Atmos. Sci.,* **44,** 2804–2812.